

A data- and compute-efficient chest X-ray foundation model beyond aggressive scaling

Chong Wang^{1,2*†}, Yabin Zhang^{1,2†}, Yunhe Gao^{1,2},
Maya Varma^{1,2,3}, Clemence Mottez^{1,2}, Faidra Patsatzi^{1,2},
Jiaming Liu^{1,2}, Jin Long^{1,4}, Jean-Benoit Delbrouck^{1,2},
Sergios Gatidis², Akshay S. Chaudhari^{1,2,5}, Curtis P. Langlotz^{1,2,5,6}

¹Stanford Center for Artificial Intelligence in Medicine and Imaging,
Stanford University, Palo Alto, CA, USA.

²Department of Radiology, Stanford University, Stanford, CA, USA.

³Department of Computer Science, Stanford University, Stanford, CA,
USA.

⁴Department of Pediatrics, Stanford University, Stanford, CA, USA.

⁵Department of Biomedical Data Science, Stanford University,
Stanford, CA, USA.

⁶Department of Medicine, Stanford University, Stanford, CA, USA.

*Corresponding author(s). E-mail(s): chongwa@stanford.edu;

†These authors contributed equally to this work.

Abstract

Foundation models for medical imaging are typically pretrained on increasingly large datasets, following a “scale-at-all-costs” paradigm. However, this strategy faces two critical challenges: large-scale medical datasets often contain substantial redundancy and severe class imbalance that bias representation learning toward over-represented patterns, and indiscriminate training regardless of heterogeneity in data quality incurs considerable computational inefficiency. Here we demonstrate active, principled data curation during pretraining can serve as a viable, cost-effective alternative to brute-force dataset enlargement. We introduce CheXficient, a chest X-ray (CXR) foundation model that selectively prioritizes informative training samples. CheXficient is pretrained on only 22.7% of 1,235,004 paired CXR images and reports while consuming under 27.3% of the total compute budget, yet achieving comparable or superior performance to its full-data counterpart and other large-scale pretrained models. We assess CheXficient across 20 individual benchmarks spanning 5 task types, including

non-adapted off-the-shelf evaluations (zero-shot findings classification and cross-modal retrieval) and adapted downstream tasks (disease prediction, semantic segmentation, and radiology report generation). Further analyses show CheX-efficient systematically prioritizes under-represented training samples, improving generalizability on long-tailed or rare conditions. Overall, our work offers practical insights into the data and computation demands for efficient pretraining and downstream adaptation of medical vision–language foundation models.

Keywords: Foundation models, medical data, efficient learning, CXR interpretation.

1 Introduction

Medical foundation models have emerged as a powerful paradigm for building general-purpose artificial intelligence systems in healthcare, offering a unified framework for learning transferable representations from massive medical data [1–3]. In medical imaging, such models have shown strong performance across diverse specialties, including radiology [4], pathology [5], dermatology [6], and ophthalmology [7], with the potential to support a wide range of clinically relevant downstream tasks. Typically, medical foundation models are pretrained on indiscriminately collected, large-scale datasets (e.g., chest X-rays and associated free-text radiology reports [8], figures with captions from scientific articles [9, 10], and social media posts [11]) to acquire highly generalizable representations, which can then be adapted to specific clinical applications using comparatively limited task-specific annotations [12].

Despite these promising achievements, the reliance on large-scale medical datasets presents significant practical challenges that limit the feasibility and sustainability of medical foundation models in real-world clinical settings. In practice, retrospective archives, data-sharing initiatives, and web-sourced medical content have made large-scale medical datasets increasingly accessible [13], yet standard pretraining approaches that blindly train on all available data face two critical inefficiencies. First, medical datasets often exhibit high redundancy and severe class imbalance [14], e.g., normal findings and common pathologies dominate while rare but clinically important conditions are under-represented, biasing representation learning toward over-represented patterns. Second, exhaustive training on millions of samples without accounting for heterogeneity in data quality incurs prohibitive computational burden [2] (e.g., RadFM [15] trained on 16M radiology scans using 32 NVIDIA A100 GPUs for weeks; MedGemma [16] trained on 33M medical image-text pairs using industrial-scale computational resources accumulating thousands of TPU-hours), creating substantial barriers for academic and clinical institutions with limited resources.

These challenges motivate exploring an alternative paradigm, rather than pursuing ever-larger datasets. Recent advances in machine learning suggest that optimizing which data are utilized for training can be more influential than simply increasing how much data is used [17]. A growing body of work [17–20] shows that training samples differ markedly in their contribution to representation learning: some examples

are highly informative, while others provide little benefit or can even hinder optimization [21]. Nevertheless, standard pretraining approaches of foundation models typically treat all data points as equally valuable, overlooking substantial differences in informativeness, representativeness, relevance, or diversity. This insight has driven a shift toward data curation or selection strategies, in which compact, high-value subsets are selectively emphasized and employed for training. Empirical evidence [18, 21–23] outside the medical domain demonstrates that models trained on carefully curated datasets can match or even surpass the performance of those trained on much larger corpora, challenging the long-standing assumption that generalization ability scales predominantly with dataset size. These findings are particularly relevant to medical imaging, where data distributions are highly imbalanced across normal findings, rare pathologies, and acquisition protocols, treating all training samples uniformly is especially inefficient and can bias representation learning toward over-represented patterns. These observations raise a central question: can medical foundation models achieve comparable or superior performance while substantially reducing data and computational requirements through systematic, principled data selection?

In this work, we introduce CheXficient, a chest X-ray (CXR) foundation model built within a contrastive language-image pretraining (CLIP [25]) framework and unprecedentedly designed to improve both data and computation efficiency through systematic data curation. As illustrated in Figure 1(a), CheXficient incorporates a prototype-driven online data curator during pretraining. A set of evolving prototypes (i.e., prototypical centroids) [26, 27] is leveraged to approximate the underlying data manifold, enabling dynamic prioritization of informative CXR image–report data pairs for model optimization. To be concrete, training samples that lie farther from the prototypes (corresponding to under-represented but informative regions of the data distribution) are emphasized, while training samples near the prototypes, which tend to contain redundant information, are down-weighted and under-sampled (Figure 1(b); see Methods). This strategy yields a compact yet comprehensive coverage of the data manifold, leading to improved data scalability and computational efficiency compared with existing vision–language pretraining approaches (Figure 1(d)). We systematically evaluate CheXficient under 5 complementary evaluation protocols (Figure 1(c)), encompassing both non-adapted tasks (zero-shot findings classification and zero-shot cross-modal retrieval) and adapted downstream tasks (multi-class disease prediction, semantic segmentation of anatomical structures and abnormalities, as well as radiology report generation). Together, these tasks reflect core clinical use cases of medical foundation models, spanning diagnostic decision support, anatomical understanding, and clinical reporting. Using only 22.7% of 1,235,004 paired CXR training samples (sourced from 13 public datasets across multiple countries (Table 1)) and under 27.3% of the full compute budget, CheXficient obtains performance on par with or superior to its full-data pretraining counterpart across 20 evaluation benchmarks (Figure 1(d, e)). In addition, CheXficient consistently outperforms existing state-of-the-art vision-language foundation models pretrained on substantially larger-scale medical data (Figure 1(d, e)).

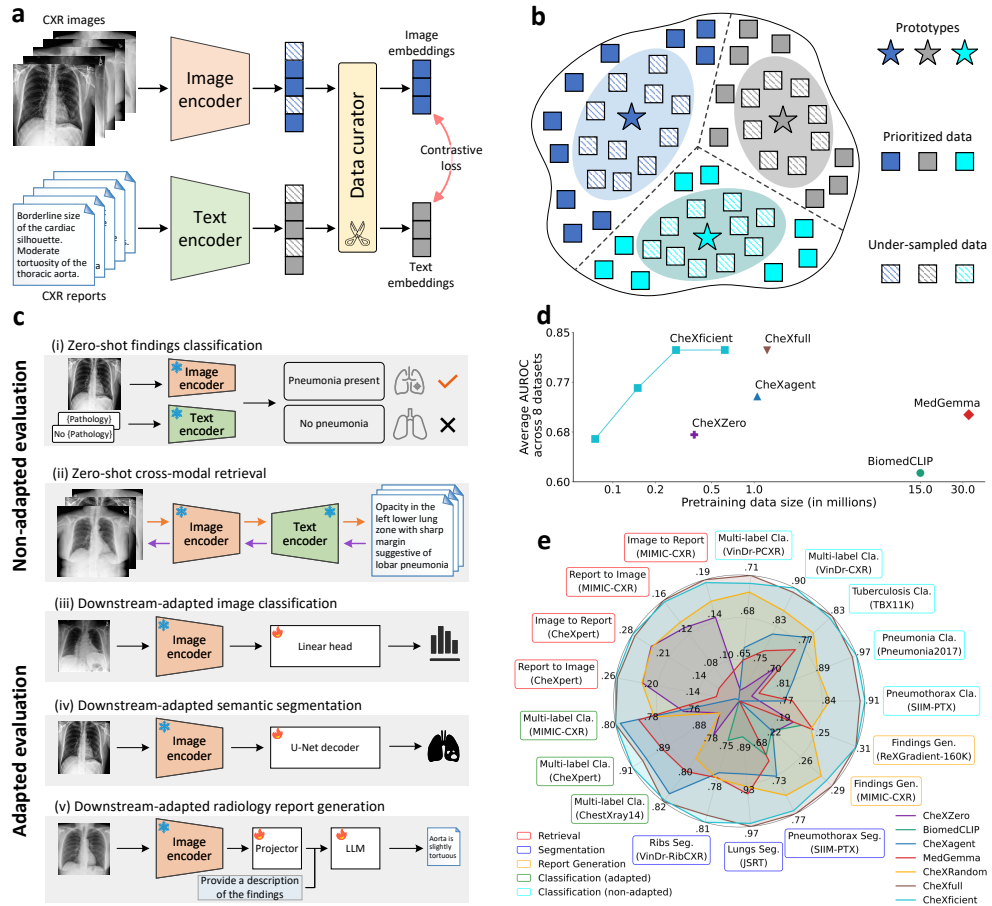


Fig. 1 Overview of this study. (a) **CheXficient pretraining strategy**. Paired chest X-ray (CXR) images and radiology reports are employed. A data curator selectively determines which image–report pairs are included in training, followed by optimization with an InfoNCE [24] contrastive loss. (b) **Data curation mechanism**. The data curator prioritizes image–report pairs based on their proximity to a set of learnable prototypes. Samples farther from the prototypes are assigned higher priority, while more redundant data closer to the prototypes is down-sampled. (c) **Evaluation protocol**. After pretraining, CheXficient is evaluated on non-adapted tasks without any architectural or weight modifications, including (i) zero-shot finding classification and (ii) zero-shot cross-modal retrieval. CheXficient can also be adapted to downstream tasks via fine-tuning, including (iii) multi-class disease prediction, (iv) semantic segmentation, and (v) radiology report generation. (d) **Data efficiency analysis**. Zero-shot findings classification performance (average AUROC on 8 datasets) versus pretraining data size compared with alternative pretraining strategies and models. (e) **Overall performance**. CheXficient achieves better or comparable performances with full-data pretraining, while greatly outperforming other existing large-scale pretrained models on diverse evaluation benchmarks spanning 5 task types: retrieval (in Recall@1), segmentation (in Dice score), and report generation (in RadGraph), adapted and non-adapted classification (in AUROC).

2 Results

2.1 Model design and experimental setup

To validate the data- and compute-efficiency of CheXficient in contrastive CXR pretraining, we construct a large-scale pretraining database containing over 1.235 million CXR image-report pairs collected from 13 publicly available sources, including CheXpert-Plus [28], MIMIC-CXR [29], ReXGradient-160K [30], PadChest [31], BIMCV COVID-19 [32], CANDID-PTX [33], CASIA-CXR [34], Open-I [35], ChestX-ray14 [36], BRAX [37], VinDr-CXR [38], VinDr-PCXR [39], and ChestDR [40]. The detailed composition of the full pretraining database is provided in Table 1.

We compare the performance of CheXficient against that of the following baseline foundation models: CheXrandom and CheXfull. To obtain a fair comparison, the same network architectures (DINOv2 [41] as the image encoder and BioClinicalBERT [42] as the text encoder), pretraining recipe (image-text contrastive learning by InfoNCE loss [24]), and evaluation protocols are employed in all models. CheXfull is pretrained on the entire 1.235 million paired CXR data. CheXficient is pretrained on a carefully curated subset from the full pretraining corpus. CheXrandom is pretrained on a random subset of the full set, with an identical size as the curated subset. We evaluate CheXficient on 20 benchmarks across two evaluation protocols: (1) non-adapted zero-shot evaluation: findings classification (47 thoracic findings) and cross-modal retrieval (image to reports, image to *Findings*, image to *Impression* and vice versa); (2) adapted downstream fine-tuning evaluation: multi-disease prediction, radiology report generation, as well as semantic segmentation of anatomic structures and abnormalities. Detailed information on downstream datasets is given in Table 2. The area under the receiver operating curve (AUROC), Recall@1, Dice score, and standard radiology report generation metrics (e.g., RadGraph) are utilized for evaluating the task performance of these models. In experiments, we train the models with different seeds to obtain multiple results and evaluate their performances for statistical analysis.

2.2 CheXficient prioritizes under-represented training data

To study and understand the characteristics of the curated training data, we extract feature embeddings for full-set and curated-set training samples, using the pretrained CheXfull model. For comparison, we additionally consider a random subset (with the same size as the curated set) used by CheXrandom. We apply principal component analysis [43] (PCA) to project the high-dimensional features (unified multimodal representation, see Section 4.4) into a two-dimensional space for visualization. Figure 2(a) illustrates the resulting feature distributions using two-dimensional histograms. The curated subset exhibits a substantially different pattern compared to both the full dataset and the random subset. Particularly, curated samples populate regions that are sparsely covered by the full dataset, suggesting an over-representation of uncommon imaging patterns, atypical report semantics, or long-tailed thoracic diseases.

To quantitatively characterize these differences, we also measure the local sample density using the average k -nearest neighbor (kNN) distance in the raw feature space. As reported in Figure 2(b), curated samples exhibit a much larger kNN distance than

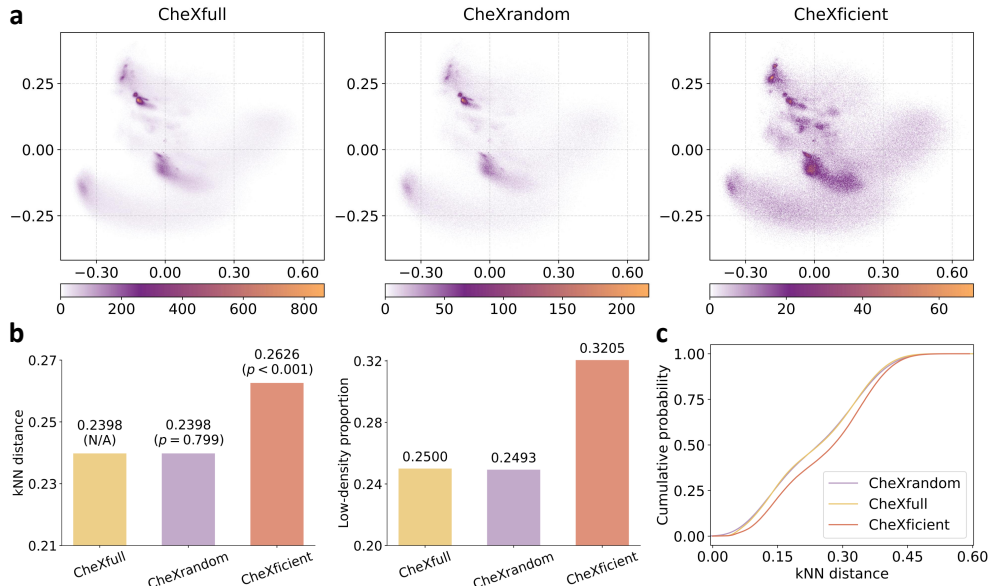


Fig. 2 (a) Feature distribution of training samples from the full set (CheXfull, $n = 1,235K$), random subset (CheXrandom, $n = 280K$), and curated subset (CheXficient, $n = 280K$). Qualitative histograms of feature embeddings projected onto a two-dimensional PCA space (Colorbars are independently normalized to reveal the structural organization of the PCA space, absolute density values are therefore not directly comparable across methods). The curated subset occupies distinct and long-tailed regions in the feature space, compared with both the full and random subsets. (b) Quantitative analysis of local feature density (left) for samples from the full set, random subset, and curated subset, measured by the average k -nearest neighbor (kNN) distance ($k = 20$) computed in the raw feature space. p -values are reported from Welch’s t-test by comparing each subset against the full set. The low-density proportion (right) denotes the fraction of samples falling within the top 25% lowest-density regions of the full dataset. (c) CDF plot of the average kNN distance. Curated samples (red) are shifted toward higher kNN distances, indicating enrichment in low-density regions, whereas the random subset (purple) closely overlaps with the full set (yellow).

the full set (0.2626 vs. 0.2398), indicating an enrichment of long-tailed and under-represented samples in low-density regions. This difference is statistically significant ($p < 0.001$). In addition, more than 32% of curated samples fall within the top 25% lowest-density regions of the full set. In Figure 2(c), the CDF (cumulative distribution function) plot of average kNN distances shows that the curated subset (red) is systematically shifted to the right, further verifying an enrichment of low-density, long-tailed samples. In contrast, a randomly sampled subset (purple) closely overlaps with the full set (yellow), demonstrating that random selection does not preferentially sample low-density regions.

2.3 Performance in non-adapted zero-shot tasks

We first assess the performance of pretrained vision-language models (CheXficient, CheXrandom, and CheXfull) on two non-adapted zero-shot tasks, where these models are directly used without any architecture or weight modifications. For zero-shot

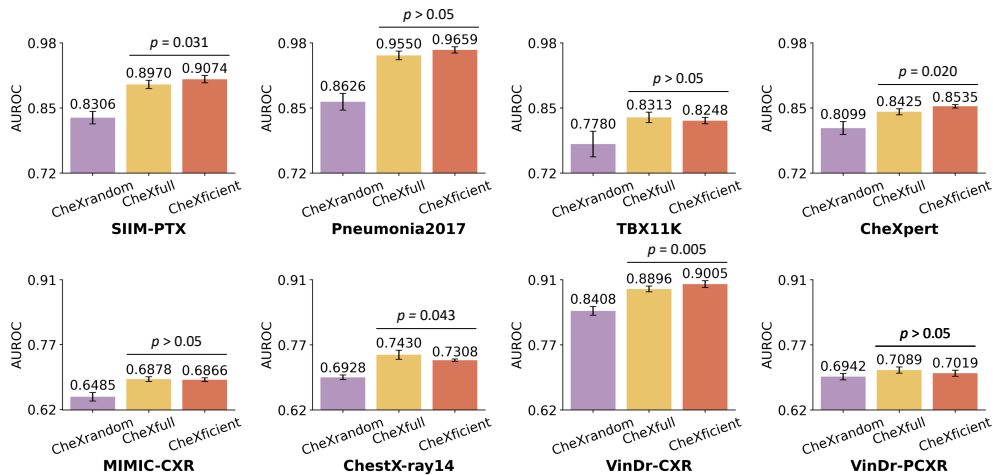


Fig. 3 Performance on zero-shot findings classification. We evaluate the pretrained models on 8 public datasets. Among them, SIIM-PTX, Pneumonia2017, and TBX11K are from external domains unseen in pretraining, while the remaining 5 datasets are used for internal evaluation. Compared to CheXfull, CheXficient achieves higher AUROC on three datasets ($p < 0.05$), comparable performance on four datasets ($p > 0.05$), and lower performance on one dataset ($p < 0.05$). Across all datasets, CheXficient achieves higher AUROC than CheXrandom. We present the mean \pm 95% confidence interval (CI) of AUROC for each model. The listed p -values are computed using two-sided t -tests.

findings classification, we follow prior work [8] and prompt the text encoder with class-specific descriptions. For zero-shot cross-modal retrieval, we employ radiology reports as queries to prompt the text encoder.

2.3.1 Zero-shot findings classification

We evaluate the pretrained CheXficient, CheXrandom, and CheXfull on the SIIM-PTX [44] dataset ($n = 1,372$), containing binary classification labels (pneumothorax vs. no pneumothorax). As shown in Figure 3, CheXficient significantly outperforms CheXfull ($p = 0.031$) and substantially exceeds the performance of CheXrandom (AUROC: 0.9074 (95% CI 0.9001, 0.9148) vs. 0.8306 (95% CI 0.8181, 0.8431)). We also evaluate the above three pretrained models on the Pneumonia2017 [45] dataset ($n = 624$), where each CXR image is labeled either pneumonia (bacterial/viral) or normal. CheXficient attains AUROC performance comparable to CheXfull, with an improvement of more than 10.3% over CheXrandom. We conduct tuberculosis classification on the TBX11K [46] dataset ($n = 1,800$), where each image is labeled either tuberculosis or non-tuberculosis. CheXficient again achieves AUROC performance comparable to CheXfull and outperforms CheXrandom.

Beyond single-disease tasks, recent research [47, 48] has focused on comprehensive detection of multiple thoracic diseases and imaging findings. We therefore evaluate CheXficient on five multi-label chest X-ray benchmarks: CheXpert [28] ($n = 500$, 14 categories), MIMIC-CXR [29] ($n = 3,082$, 14 categories), ChestX-ray14 [36] ($n = 25,596$, 15 categories), VinDr-CXR [38] ($n = 3,000$, 28 categories), and VinDr-PCXR [39] ($n = 1,397$, 15 categories) datasets. For each dataset, we compute

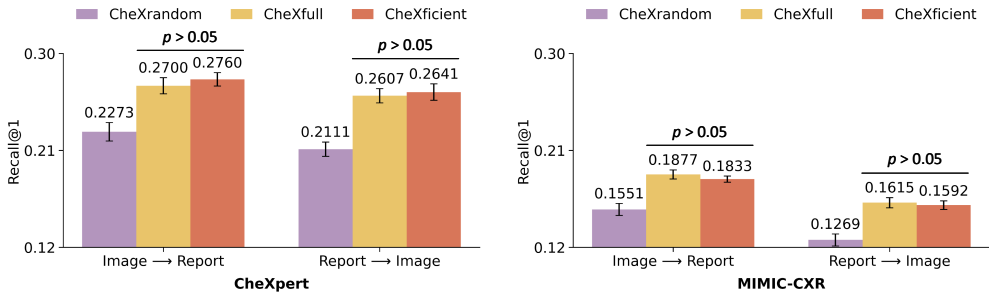


Fig. 4 Performance on zero-shot cross-modal retrieval. We evaluate the pretrained models on the public CheXpert and MIMIC-CXR benchmarks. CheXficient achieves performance comparable to CheXfull on both datasets ($p > 0.05$), while outperforming CheXrandom. We report the mean \pm 95% CI of Recall@1 (The recall of retrieving the exact paired CXR report (or image) within the top-1 result for a given CXR image (or report)).

category-wise AUROC and report the macro-average. CheXficient achieves a higher macro AUROC than CheXfull on CheXpert ($p = 0.020$) and VinDr-CXR ($p = 0.005$), while yielding comparable performance on MIMIC-CXR and VinDr-PCXR, and lower performance on ChestX-ray14. Across all five benchmarks, CheXficient consistently achieves higher AUROC than CheXrandom.

Notably, three datasets (SIIM-PTX, Pneumonia2017, and TBX11K) originate from institutions and data distributions entirely disjoint from the pretraining corpus and are therefore treated as external evaluation benchmarks (Table 2). As shown in Figure 3, CheXficient achieves performance comparable to or exceeding CheXfull across these unseen domains, despite being pretrained on less data. AUPRC results on the 8 public datasets are reported in Extended Data Figure 1.

2.3.2 Zero-shot cross-modal retrieval

Zero-shot cross-modal retrieval aims to evaluate a model’s ability to match a CXR image to its corresponding radiology report (*Findings* section, *Impressions* section, or their combination) and vice versa. As illustrated in Figure 4, CheXficient obtains performances on par with CheXfull and surpasses CheXrandom, on the task of retrieving the correct CXR report for a given CXR image (Image \rightarrow Report) across both evaluation datasets (CheXpert ($n = 1,000$) and MIMIC-CXR ($n = 3,082$)). A similar trend is observed for retrieving the correct CXR image given a CXR report (Report \rightarrow Image). In this evaluation, *Findings* and *Impressions* sections are combined to form the textual report, retrieval results based solely on either section are provided in Extended Data Figure 2 and Figure 3.

2.3.3 Pretraining data and compute efficiency

We validate the importance and advantage of active curation by assessing the pretraining data and compute efficiency, defined as the amount of paired image-report data and pretraining time (GPU-hours) required to build a high-performing CXR foundation model.

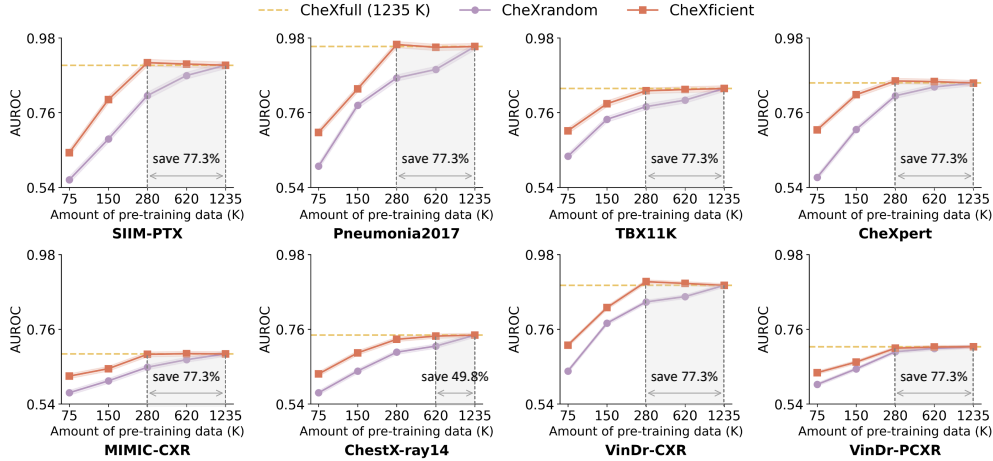


Fig. 5 Zero-shot findings classification performance under different pretraining data budgets. The performance of both CheXficient and CheXrandom progressively increases on all 8 benchmarks as the quantity of pretraining samples increases. CheXficient consistently outperforms CheXrandom at all data budgets and across all benchmarks, demonstrating higher data efficiency. When pretrained on only 280K curated image-report pairs (22.7% of the full data, except for ChestX-ray14), CheXficient performs better or similarly to the full-data pretrained model CheXfull.

We compare CheXficient with the baseline CheXrandom model, which is trained under identical pretraining data budgets ranging from 75K to 1.235M image-report pairs. Figure 5 shows zero-shot findings classification performance across different pretraining set sizes, with the CheXfull model (trained on the entire dataset) included as a reference. The performance of both models consistently improves across the eight evaluation benchmarks as the size of the pretraining corpus increases. Across all data budgets and benchmarks, CheXficient achieves higher performance than CheXrandom. When pretrained on 280K curated image-report pairs (22.7% of the full data), CheXficient achieves performance comparable to CheXfull on SIIM-PTX, Pneumonia2017, CheXpert, MIMIC-CXR, and VinDr-CXR.

We further investigate the pretraining compute efficiency in the context of zero-shot findings classification. Computational cost is quantified in NVIDIA H100 GPU-hours. For a fair comparison, all models are pretrained for the same total number of epochs (20 epochs), which we found sufficient for convergence. CheXfull is pretrained on the entire dataset comprising 1.235 million image-report pairs, whereas CheXrandom and CheXficient are pretrained on the same subset size (280K). As shown in Figure 6, CheXficient achieves comparable or superior performance while requiring substantially less pretraining time, saving 72.7–81.8% of H100 GPU-hours relative to CheXfull, which requires 220 H100 GPU-hours. Under matched pretraining computational budgets, CheXficient consistently outperforms CheXrandom across all of the eight evaluation benchmarks.

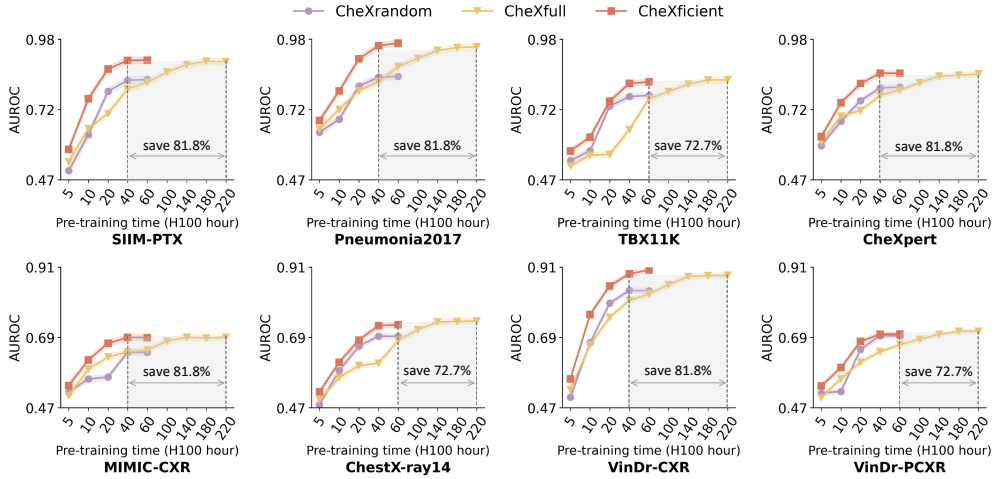


Fig. 6 Zero-shot findings classification performance under different pretraining computation budgets. The three models are pretrained for the same number of epochs. CheXficient (280K) consistently outperforms CheXrandom (280K) and CheXfull (1235K) on all evaluation benchmarks when using the same pretraining time, highlighting the compute efficiency of curated pretraining of CheXficient.

2.4 Performance in adapted downstream tasks

We next evaluate the performance of pretrained vision–language models (CheXficient, CheXrandom, and CheXfull) on three adapted downstream tasks: image classification, semantic segmentation, and radiology report generation. In all tasks, the pretrained image encoder is leveraged as a fixed feature extractor, while task-specific heads or decoders are appended and fine-tuned on target labeled datasets. Detailed fine-tuning configurations are provided in Appendix C.

2.4.1 Classification label efficiency and fine-tuning performance

To assess the representation quality learned through efficient pretraining in CheXficient, we evaluate downstream image classification (disease prediction) performance on three representative multi-label CXR datasets: CheXpert, MIMIC-CXR, and ChestXray14, which cover a diverse set of anatomical and pathological findings and diseases. We adopt a linear-probing protocol with a frozen image encoder backbone. Specifically, a randomly initialized linear classification head is attached to the pretrained image encoder, and only this linear classifier is trained using images and corresponding labels from the target dataset. For comparison purposes, we also include DINOv2 [41], which is pretrained solely on 142 million natural images.

As shown in Figure 7, AUROC performance of all models increases with the amount of labeled data used for fine-tuning. Models pretrained on CXR data achieve higher performance than DINOv2. Across different proportions of labeled training data, CheXficient realizes performance comparable to CheXfull. CheXficient achieves performance comparable to CheXrandom while using approximately 10% of the labeled training samples. The AUPRC results of CheXficient are also similar to those of

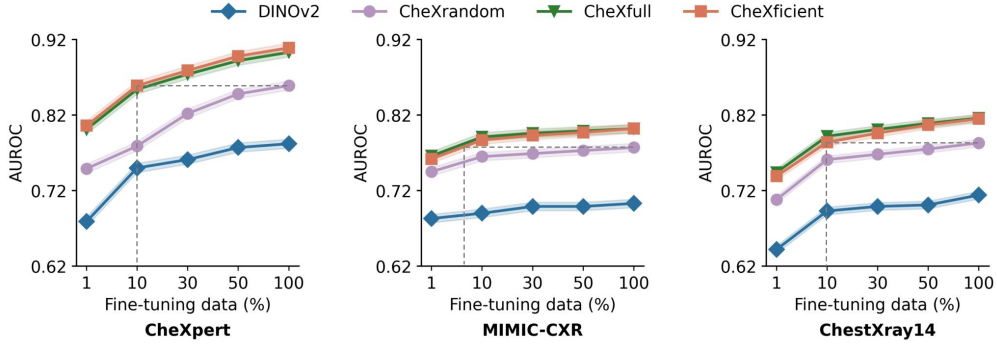


Fig. 7 Comparison of CheXefficient with other pretrained models in label-efficient disease prediction across three representative datasets: CheXpert ($n = 500$, 14 categories), MIMIC-CXR ($n = 3,082$, 14 categories), and ChestXray14 ($n = 25,596$, 15 categories). Performance is reported at varying proportions of labeled training data. Vertical dashed lines indicate the amount of labeled data required for CheXefficient to match the performance of its counterpart CheXrandom.

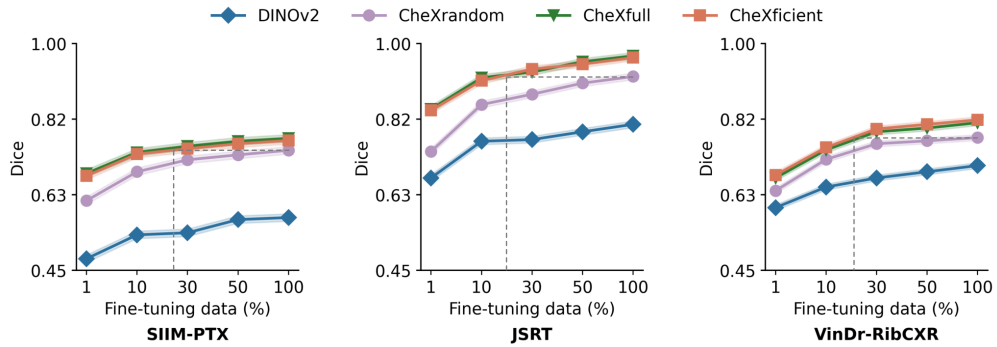


Fig. 8 Comparison of CheXefficient with other pretrained models in annotation-efficient anatomical and pathological segmentation across three datasets: SIIM-PTX ($n = 1,372$), JSRT ($n = 50$), and VinDr-RibCXR ($n = 49$). Performance is reported at varying proportions of annotated training samples. Vertical dashed lines indicate the amount of annotated data required for CheXefficient to match the performance of its counterpart CheXrandom.

CheXfull on these three datasets (Extended Data Figure 4). Furthermore, CheXefficient also outperforms other large-scale pretrained models (e.g., BiomedCLIP [9] and MedGemma [16]) that are trained on more than $50\times$ the amount of data used by CheXefficient (see Figure 1(e) and Extended Data Table 1), underscoring the advantages of active and principled data curation over sheer dataset scaling.

2.4.2 Segmentation annotation efficiency and fine-tuning performance

To further evaluate the quality of dense representations learned through curated pre-training, we focus on downstream tasks of semantic segmentation. Specifically, we consider three commonly adopted CXR benchmarks covering both pathological and anatomical structures: pneumothorax segmentation on SIIM-PTX [44], lung segmentation on JSRT [49], and rib segmentation on VinDr-RibCXR [50]. We employ a frozen

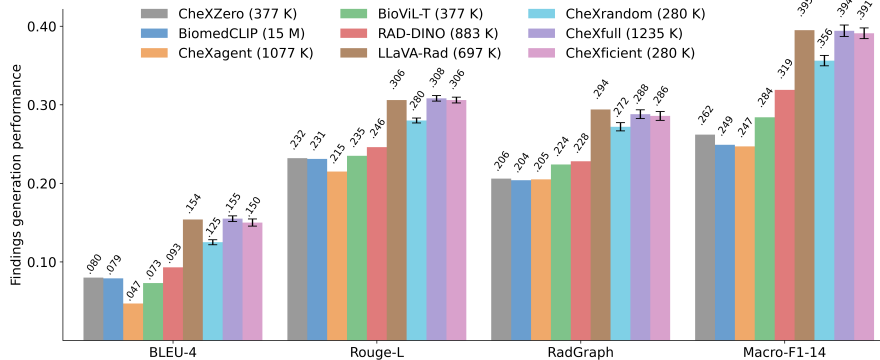


Fig. 9 Downstream radiology report (*Findings* section) generation performance (%) on official test split of MIMIC-CXR ($n = 2,461$). Text in parentheses denotes the pretraining data size of the model.

image encoder backbone within an encoder–decoder segmentation framework. A U-Net [51] decoder is attached to the pretrained image encoder and fine-tuned using CXR images and their corresponding pixel-wise annotations from each target dataset, while the image encoder remains fixed. This setup allows us to assess the quality and transferability of learned representations for pixel-level dense prediction tasks.

As shown in Figure 8, CheXficient achieves segmentation performance comparable to CheXfull across all three tasks. CheXficient exhibits strong annotation efficiency, matching the performance of CheXrandom while using 10–30% of the densely-annotated training samples. These results demonstrate that curated, data-efficient pretraining enables the learning of high-quality image representations that transfer effectively to challenging downstream segmentation tasks. CheXficient also achieves performance competitive with other off-the-shelf pretrained image encoders (e.g., BiomedCLIP [9], MedGemma [16], and CheXagent [52]), in spite of being trained on substantially smaller-scale pretraining datasets (Figure 1(e)).

2.4.3 Radiology report generation

We also evaluate the quality of image representations learned through efficient pretraining on a vision–language downstream task, namely radiology report generation for the *Findings* section. For the model architecture, we adopt a LLaVA-style multimodal framework [53]. To generate the output report, patch embeddings extracted from the frozen image encoder are projected and concatenated with a textual instruction: “Provide a description of the findings in the radiology image given the following Indication: $\langle \rangle$.” If the Indication information is unavailable, the optional $\langle \rangle$ field is omitted. Consistent with LLaVA-Rad [54], we employ a two-layer fully connected (MLP) projector and Vicuna-7B-v1.5 [55] as the language model. The projector network is randomly initialized and jointly trained with the language decoder, while the image encoder remains frozen. Performance is quantified using standard lexical metrics (BLEU-4 [56], Rouge-L [57]) and radiology-specific metrics, including RadGraph [58] and CheXbert-based Macro-F1-14 [28] (mapping “uncertain” labels to negative). For ReXGradient-160K, we additionally report RadCliQ [59], RaTEScore [60], and BertScore [61].

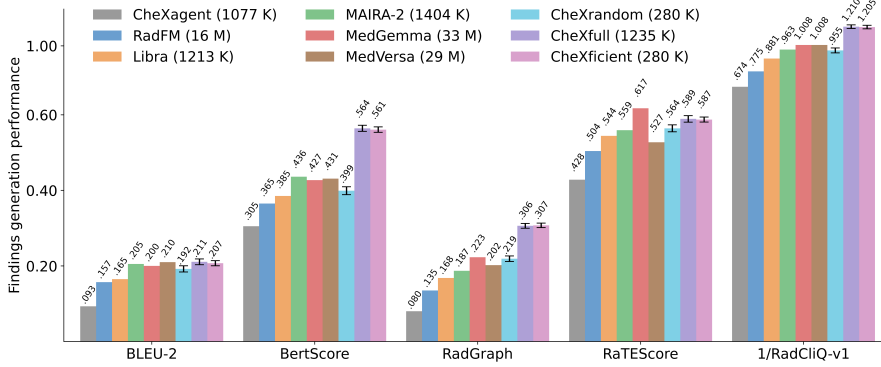


Fig. 10 Downstream radiology report (*Findings* section) generation performance (%) on official test split of ReXGradient-160K ($n = 10,000$). Text in parentheses denotes the pretraining data size of the model.

CheXficient consistently outperforms CheXrandom across all lexical and clinical metrics on both MIMIC-CXR (Figure 9) and ReXGradient-160K (Figure 10). Despite being pretrained on substantially fewer image-report pairs, CheXficient achieves performance comparable to CheXfull. On MIMIC-CXR, CheXficient slightly underperforms the recent leading report generation framework LLaVA-Rad, while demonstrating improvements over other specialized vision-language baselines, including BiomedCLIP, CheXagent, and RAD-DINO [62], all of which are pretrained on much larger-scale datasets (Extended Data Table 1). On ReXGradient-160K, CheXficient further outperforms advanced medical foundation models, e.g., RadFM [15], Libra [63], MAIRA-2 [64], and MedVersa [65].

2.5 Tackle long-tailed thoracic diseases

Chest radiograph interpretation is inherently a long-tailed problem [47, 48]. The distribution of thoracic findings is heavily skewed toward a small number of common abnormalities, as many clinically relevant conditions occur infrequently. This severe class imbalance poses substantial challenges for model learning, as training objectives are often dominated by majority classes. Consequently, AI models tend to exhibit biased representations that favor common findings, potentially at the expense of under-represented conditions. Robustness and generalizability under long-tailed distributions therefore constitute critical criteria for evaluating medical foundation models.

To investigate how active data curation during pretraining influences long-tailed generalization, we analyze the relationship between disease label distributions in the pretraining data and zero-shot generalization ability on test data. We focus on VinDr-CXR [38], as it provides comprehensive disease-level annotations covering a total of 28 findings and diagnoses, with long-tailed distributions. Specifically, we first compute the disease label distributions in the VinDr-CXR training set (see Figure 11(Top)). Then, we compare the per-category zero-shot classification performance (AUROC) on the VinDr-CXR test data for different models (Figure 11(Bottom))

We observe that *No finding* samples dominate the non-curated training sets used by CheXfull and CheXrandom. In contrast, CheXficient greatly reduces the proportion of

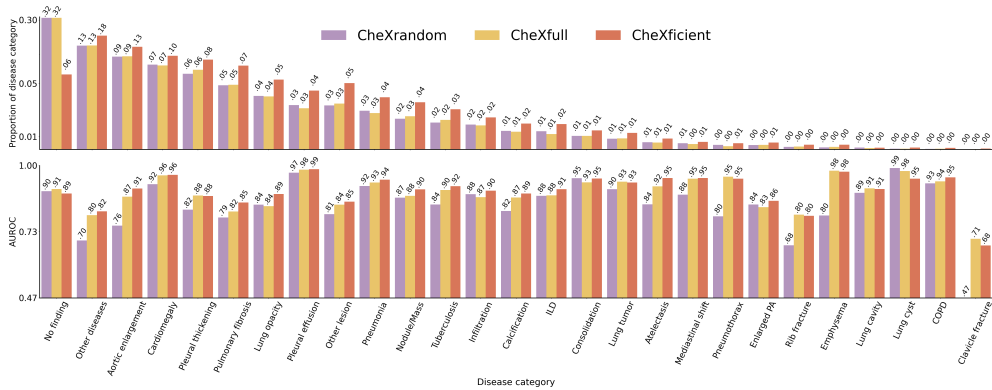


Fig. 11 Impact of curated pretraining on per-disease generalization in VinDr-CXR. Top: disease label distributions from the VinDr-CXR training set (the y-axis uses a symmetric logarithmic scale to visualize disease label frequencies spanning multiple orders of magnitude). Bottom: corresponding zero-shot per-disease AUROC results on the VinDr-CXR test set. Curated pretraining (CheXficient) re-balances label distributions and yields improved zero-shot generalization for most disease categories compared to non-curated pretraining (CheXfull and CheXrandom). Note that the disease label ‘edema’ is not shown in the figure as there are no samples with this label in the official test data.

No finding samples through active curation, while almost preserving the generalization performance for this category on the test set. Meanwhile, the curated pretraining set increases the relative prevalence of most disease labels, which is accompanied by improved zero-shot generalization across a broad range of pathologies (16 out of 26), such as *Other diseases*, *Aortic enlargement*, *Pulmonary fibrosis*, *Lung opacity*, *Pleural effusion*, *Other lesion*, and *Pneumonia*. However, this trend does not consistently hold for a small number of extremely-rare diseases, such as *Lung cyst* and *Clavicle fracture*, which each account for less than 0.1% of the training data. We hypothesize that, despite being relatively up-weighted by active curation, the absolute number of samples for these conditions remains insufficient to support robust representation learning. This observation suggests a potential limitation of data curation strategies alone in addressing long-tailed distributions and highlights that complementary approaches, such as targeted data acquisition or task-specific augmentation, may be necessary for extremely-rare disease modeling.

We further examine the adaptability of CheXficient to long-tailed conditions under limited supervision by finetuning the pretrained models with a linear-probing configuration, using only 1–5 labeled samples (*k*-shot learning) [47]. Figure 12 presents box plots of AUROC distributions for three representative VinDr-CXR conditions. CheXficient outperforms CheXfull, achieving higher median and maximum AUROC scores for *Calcification* and *Enlarged PA*, and comparable performance for *Rib fracture*. These results demonstrate that CheXficient can leverage scarce labeled data to detect long-tailed conditions, underscoring its practical value in data-scarce environments.

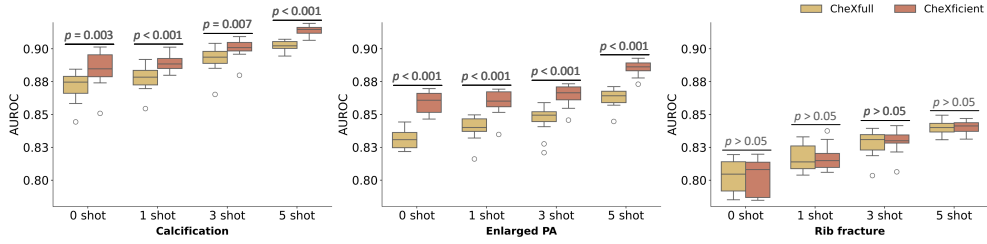


Fig. 12 Adaptability of CheXficient in detecting long-tailed conditions (Calcification, Enlarged PA (pulmonary artery), and Rib fracture) under a two-way (no finding versus each long-tailed condition) k -shot learning setting. The results demonstrate the ability of CheXficient to adapt to data-scarce conditions using only a few labeled training samples. Box plots show AUROC distributions over 20 experimental replicates, with the median (central line), interquartile range (box indicating the 25th and 75th percentiles), whiskers extending to 1.5 times the interquartile range, and outliers shown as individual points. p -values from two-sided t -tests are reported.

3 Discussion

In this study, we propose a data- and compute-efficient pretraining approach for medical foundation models that leverages active, principled, and intelligent data curation. Rather than indiscriminately enlarging training datasets [66, 67] and incurring substantial computational costs, our approach optimizes the utilization of data and compute budgets during pretraining, offering a cost-effective alternative for building high-performing medical foundation models. By curating 280K image-report pairs (22.7%) from a pool of 1.235 million paired CXR images and radiology reports, we pretrained a new CXR foundation model, CheXficient. Extensive experiments demonstrate that CheXficient achieves comparable or superior performance to a full-data pretrained counterpart across diverse evaluation benchmarks spanning 5 evaluation protocols. These evaluations cover both non-adapted tasks, including zero-shot findings classification and zero-shot cross-modal retrieval, as well as adapted downstream tasks such as multi-label disease prediction, semantic segmentation of anatomical structures and abnormalities, and radiology report generation. Together, these results provide strong evidence that curated pretraining on large-scale medical datasets can substantially improve data and compute efficiency as well as generalizability, without sacrificing overall performance. We also analyze feature distributions of the curated training samples (Figure 2). The curated data exhibits distinctive local sample-density structures, reflecting its ability to preserve data diversity while emphasizing under-represented and informative samples. This structural property is closely associated with strong model performance (Figure 3 and Figure 4) and improved long-tailed generalization (Figure 11 and Figure 12) in the resulting CXR foundation model.

In the pretraining phase, CheXficient integrates an online data curator that employs a set of evolving prototypes (i.e., prototypical centroids) to approximate the global data manifold. The curator selectively prioritizes informative CXR image-report pairs for model optimization: samples that lie far from the learned prototypes are emphasized, while those close to the prototypes are down-weighted and under-sampled. Those unselected samples are excluded from the pretraining process. In comparison with CheXfull, which shares an identical network architecture but is

pretrained on the entire training set of 1.235 million data pairs, CheXficient achieves substantially higher pretraining data efficiency (Figure 5). In addition, CheXficient requires significantly less pretraining computational cost than CheXfull (Figure 6).

Despite being pretrained on only 280K image-report pairs, CheXficient demonstrates strong and consistent performance across a wide range of downstream applications, including both unimodal evaluations (image classification and semantic segmentation) and multimodal tasks such as radiology report generation. Across eight datasets, CheXficient achieves performance comparable to or exceeding that of CheXfull (Figures 7, 8, 9, and 10). Another appealing capability of CheXficient is its ability to reduce the amount of expert-annotated training data required for downstream tasks. Figure 7 demonstrates the high labeling efficiency of CheXficient in terms of image classification. On the MIMIC-CXR dataset, it achieves the classification performance of CheXrandom (pretrained on a random subset with an identical size as the curated subset), using less than 10% of the labeled finetuning data. A similar trend is observed for downstream semantic segmentation tasks (Figure 8). Furthermore, CheXficient shows highly competitive results of radiology report generation compared with other large-scale pretrained models (Figure 9 and Figure 10).

We further conducted analyses on patient demographic characteristics, including age and race. We observed that the curated subset contains a relatively higher proportion of training samples from two age groups: pediatric patients (0–5 years), whose CXRs exhibit greater anatomical variability, and older adults (over 65 years), whose CXRs often present a broader spectrum of age-related pathologies due to their higher prevalence in this population (Appendix A.1). Regarding patient race, the data curation process does not exhibit noticeable bias, and the racial distribution remains comparable between the curated subset and the full training set (see Appendix A.2). In addition, the curation process exhibits a mild preference for frontal CXR scans over lateral CXR scans (Appendix A.3), as frontal CXRs may provide more informative visual cues for many radiological findings. It also demonstrates a pronounced preference for samples with longer CXR reports (Appendix A.4), which are prone to contain richer and more detailed clinical descriptions. Combined with the observations from Figure 11, these results inspire an important and broad implication: data acquisition or collection practices for developing medical foundation models may benefit from prioritizing under-represented data, long-tailed populations, and informative samples with rich visual and textual clinical content.

Despite promising results, we acknowledge several limitations in our methodology and evaluations. First, due to the limited scope of our study, we have not studied alternative encoder architecture adaptations, e.g., ViT-Large architecture adopted by other CXR foundation models (Extended Data Table 1). We expect that incorporating more advanced encoder architectures into our framework could yield additional performance gains due to enhanced representational capacity, and we leave this exploration for future work. Second, our multimodal evaluation is currently limited to textual report generation. Other important radiological multimodal tasks, such as visual question answering [68, 69] and visual grounding [70], remain unexplored and represent promising directions for future research. Third, although our validation covers 47 thoracic findings and diseases across major categories (e.g., cardiomegaly, pneumonia,

and nodule), this constitutes only a fraction of known thoracic conditions (for example, over 170 radiographic findings reported in [31]), with limited coverage of rare diseases and complex systemic diseases. Future studies should aim for broader and more comprehensive evaluation across a wider spectrum of thoracic conditions.

In summary, we present a data- and compute-efficient CXR foundation model based on active, principled, and intelligent data curation. Under non-adapted evaluation settings, CheXficient demonstrates strong zero-shot generalization performance while achieving high pretraining data and computation efficiency. When adapted to a range of downstream tasks, CheXficient consistently exhibits high labeling and fine-tuning efficiency without compromising performance. Overall, our work highlights the potential for substantial cost savings through strategic dataset acquisition that prioritizes informative and long-tailed data, and provides valuable insights for medical domains where the development of foundation models has been constrained by limited access to large-scale annotated data and extensive computational resources.

4 Methods

4.1 Datasets for pretraining

We construct a large-scale pretraining corpus comprising over 1.235 million paired CXR-report samples, which are collected and aggregated from 13 publicly available datasets covering diverse patient populations worldwide, including MIMIC-CXR [29], CheXpert Plus [28], ReXGradient-160K [30], PadChest [31], BIMCV COVID-19 [32], CANDID-PTX [33], CASIA-CXR [34], Open-I [35], ChestX-ray14 [36], BRAX [37], VinDr-CXR [38], VinDr-PCXR [39], and ChestDR [40]. The detailed composition and distribution of the full dataset are summarized in Table 1. This diverse aggregation enables broad coverage of imaging protocols, disease spectra, and textual reporting styles, which is critical for robust and generalizable representation learning. To ensure transparency and reproducibility, we strictly follow the official train/validation/test splits provided by each dataset when available, and incorporate only the train split into the pretraining corpus.

Among the 13 contributing datasets, 8 provide raw radiology reports, including MIMIC-CXR [29], CheXpert Plus [28], ReXGradient-160K [30], PadChest [31], BIMCV COVID-19 [32], CANDID-PTX [33], CASIA-CXR [34], and Open-I [35]. Notably, several of these datasets (PadChest, BIMCV COVID-19, and CASIA-CXR) contain non-English reports, which are automatically translated into English to ensure linguistic consistency across the corpus. For all datasets with reports, regex-based filtering is applied to handle common formatting inconsistencies such as repeated whitespace and malformed line breaks. Samples in which both the *Findings* and *Impression* sections are blank are excluded from the corpus.

The remaining 5 datasets do not include free-text reports but instead provide structured diagnostic labels (e.g., pleural effusion, cardiomegaly, atelectasis). They are ChestX-ray14 [36], BRAX [37], VinDr-CXR [38], VinDr-PCXR [39], and ChestDR [40]. For these datasets, we generate pseudo-reports using a template-based report synthesis

strategy introduced in prior work [54]. The resulting synthetic reports exhibit a token-length distribution comparable to that of real-world reports (Table 1) and account for only a small portion (12.6%) of the overall pretraining corpus.

Table 1 An extensive corpus of 1.235 million CXR image-report pairs employed for model pretraining in our experiments. We exclude images that do not belong to standard views (i.e., frontal or lateral). Real-world *Findings* are extracted from the free-text radiology reports. Synthetic *Findings* are generated using template sentences derived from clinical diagnostic labels.

Source dataset	Country	Patients	Labels	Text tokens			Image-text pairs
				5%-ile	Average	95%-ile	
<i>Real-world Findings (87.4%)</i>							
MIMIC-CXR	U.S.	65,379	–	42	94	176	354,619
ReXGradient-160K	U.S.	95,716	–	35	76	152	238,965
CheXpert-Plus	U.S.	64,725	–	38	98	209	222,116
PadChest	Spain	67,625	–	6	30	76	160,672
BIMCV-COVID19	Spain	25,082	–	8	46	102	65,421
CANDID-PTX	New Zealand	13,744	–	8	42	97	19,609
CASIA-CXR	France	11,111	–	57	96	145	11,111
Open-I	U.S.	3,996	–	29	72	139	7,424
<i>Synthetic Findings (12.6%)</i>							
NIH ChestX-ray14	U.S.	28,008	15	17	72	159	86,524
BRAX	Brazil	18,442	14	11	29	65	40,967
VinDr-CXR	Vietnam	15,000	28	17	107	325	15,000
VinDr-PCXR	Vietnam	7,728	15	17	72	189	7,728
ChestDR	China	4,848	19	20	122	239	4,848
Total:							1,235,004

4.2 Datasets for non-adapted zero-shot tasks

As shown in Table 2, non-adapted zero-shot findings classification is evaluated on the official test sets of 8 datasets: MIMIC-CXR [29], CheXpert [28], ChestX-ray14 [36], VinDr-CXR [38], VinDr-PCXR [39], TBX11K [46], SIIM-PTX [44], and Pneumonia2017 [45]. Since the pretraining pool assembles multiple public datasets, some of which (MIMIC-CXR, CheXpert, ChestX-ray14, VinDr-CXR, VinDr-PCXR) are also used for evaluation, we strictly follow the official test splits for these datasets, ensuring patient-level separation between pretraining and evaluation. This precaution addresses potential data leakage, which is the first consideration in our experiments. Notably, SIIM-PTX [44], Pneumonia2017 [45], and TBX11K [46] are unseen out-of-distribution datasets, with their test sets completely disjoint from the pretraining sources, and are therefore treated as external evaluation. Following the zero-shot classification protocol in CheXzero [8], for each disease label (e.g., mass, edema, atelectasis), we leverage the prompts “{ disease }” and “no { disease }” as positive and negative prompts for the text encoder, obtaining softmax-based probabilistic predictions.

For the non-adapted zero-shot cross-modal retrieval, evaluation is performed on two datasets: MIMIC-CXR and CheXpert. On MIMIC-CXR, the standard test split is utilized. Since CXR reports are unavailable for the CheXpert test split, we instead use CheXpert5x200 [71, 72] for the retrieval evaluation. To prevent data leakage, all the 1000 paired CXR samples in CheXpert5x200 are excluded from the pretraining pool in advance, ensuring a fair and disjoint evaluation set.

Table 2 Summary of the evaluation datasets used in this study. We evaluate on a total of 11 datasets (6 seen datasets for internal evaluation and 5 unseen datasets for external evaluation), comprising diverse evaluation benchmarks across 5 task types. We follow the official train/test splits provided by each dataset, except for CheXpert, where 1,000 paired CXR samples were excluded from the training set for retrieval evaluation.

Dataset	Learning setup	Task	Clinical conditions	# Train	# Test
<i>Internal evaluation</i>					
MIMIC-CXR	Non-adapted	Classification	14 thoracic findings	0	3,082
	Non-adapted	Retrieval	–	0	3,082
	Adapted	Classification	14 thoracic findings	227,459 (1–100%)	3,082
	Adapted	Report generation	–	146,909	2,461
CheXpert	Non-adapted	Classification	14 thoracic findings	0	500
	Non-adapted	Retrieval	–	0	1,000
	Adapted	Classification	14 thoracic findings	223,414 (1–100%)	500
NIH ChestX-ray14	Non-adapted	Classification	15 thoracic findings	0	25,596
	Adapted	Classification	15 thoracic findings	86,524 (1–100%)	25,596
VinDr-CXR	Non-adapted	Classification	28 thoracic findings	0, k -shot	3,000
VinDr-PCXR	Non-adapted	Classification	15 thoracic findings	0	1,397
ReXGradient-160K	Adapted	Report generation	–	140,000	10,000
<i>External evaluation</i>					
SIIM-PTX	Non-adapted	Classification	Pneumothorax	0	1,372
	Adapted	Segmentation	Pneumothorax	10,675 (1–100%)	1,372
Pneumonia2017	Non-adapted	Classification	Pediatric pneumonia	0	624
TBX11K	Non-adapted	Classification	Tuberculosis	0	1,800
JSRT	Adapted	Segmentation	Lungs	172 (1–100%)	50
VinDr-RibCXR	Adapted	Segmentation	Ribs	196 (1–100%)	49

4.3 Datasets for adapted downstream tasks

For adapted downstream classification tasks, evaluations are performed on the official test sets of MIMIC-CXR, CheXpert, and ChestX-ray14 (Table 2), as in the zero-shot setting. The key difference is that varying percentages (1–100%) of data from the training split are used from each dataset to fine-tune the linear classification head.

For adapted downstream image segmentation tasks, the SIIM-PTX [44], JSRT [49], and VinDr-RibCXR [50] datasets are employed for fine-tuning and evaluation, with the official data splits summarized in Table 2.

For downstream-adapted radiology report generation tasks, fine-tuning and evaluation are performed on the official splits of MIMIC-CXR and ReXGradient-160K. Following the protocols of LLaVA-Rad [54] and RAD-DINO [62], non-frontal images and samples without a *Findings* section are excluded, forming 146,909 training, 7,250 validation, and 2,461 testing image–text pairs for MIMIC-CXR. A similar pre-processing pipeline is applied to ReXGradient-160K, yielding 140,000, 10,000, and 10,000 image–text pairs for training, validation, and testing, respectively.

4.4 Active data curation in pretraining

Our CheXficient adopts a contrastive language–image pretraining framework based on CLIP [25] to actively curate informative and diverse training samples from a large-scale corpus containing over 1.235M paired CXR image–report samples. Unlike conventional pretraining pipelines that treat all samples equally, CheXficient performs online data curation during training, dynamically identifying samples that are most beneficial for the representation learning. This strategy enables efficient utilization of large-scale medical datasets, which are often redundant, imbalanced, and noisy, while substantially reducing computational cost. Formally, we consider a large image–text dataset $\mathcal{D} = \{(x_i^{\text{img}}, x_i^{\text{txt}})\}_{i=1}^{|\mathcal{D}|}$, where each data pair consists of a CXR image x_i^{img} and its corresponding textual radiology report x_i^{txt} . Our objective is to construct a compact yet representative subset $\mathcal{D}_c \subset \mathcal{D}$ during pretraining, such that a vision–language model trained on \mathcal{D}_c achieves performance comparable to training on the full dataset \mathcal{D} , but with significantly fewer samples and lower training cost.

The overall curation and pretraining procedure consists of the following steps:

- (1) **Multimodal embedding.** During pretraining, we randomly sample a large super-batch of paired CXR data $\mathcal{S} = \{(x_i^{\text{img}}, x_i^{\text{txt}})\}_{i=1}^{|\mathcal{S}|}$ from the full pretraining set \mathcal{D} . Each radiology report x_i^{txt} is tokenized and encoded by the text encoder θ_{txt} to obtain a text embedding $\mathbf{z}_i^{\text{txt}}$. Correspondingly, each CXR image x_i^{img} is resized and processed by the image encoder θ_{img} to extract an image embedding $\mathbf{z}_i^{\text{img}}$ of the same dimensionality. Both embeddings are ℓ_2 -normalized to ensure scale consistency and then concatenated to form a unified multimodal representation $\mathbf{z}_i = \text{concat}(\mathbf{z}_i^{\text{img}}, \mathbf{z}_i^{\text{txt}})$, capturing complementary semantic information from both visual and textual modalities (see ablations in Appendix B.1), which is used for subsequent data selection.
- (2) **Prototype-driven selection.** The model maintains a set of evolving prototypes $\{\mathbf{p}_k\}_{k=1}^K$ that characterize representative multimodal patterns in the data manifold (Figure 1(b)). For each concatenated embedding in \mathcal{S} , we compute its distance to the nearest prototype and rank samples accordingly. Samples that lie far from their assigned prototypes are more likely to correspond to rare pathologies, atypical imaging appearances, or under-represented report semantics, and are therefore highly informative. Accordingly, we retain a small fraction (e.g., the top 10%) of these distant samples to emphasize hard and informative examples. For the remaining majority of samples (e.g., 90%), which tend to be redundant and clustered around common patterns, we under-sample

a fixed number of data (e.g., $N = 10$) within each prototype cluster to preserve diversity. This under-sampling step is implemented using farthest point sampling [73], enhancing coverage of the feature space.

- (3) **Contrastive learning.** The selected samples constitute a mini-batch $\mathcal{M} \subset \mathcal{S}$, which is added to the curated subset \mathcal{D}_c . Given the mini-batch \mathcal{M} , we optimize the model using the InfoNCE contrastive loss [24], jointly updating the image and text encoders. This objective encourages matched CXR image-report pairs to have aligned representations, while pushing apart mismatched pairs, thereby improving cross-modal alignment and semantic consistency.
- (4) **Prototype update.** The prototypes are updated concurrently with model training to reflect the evolving data distribution. Specifically, new prototype representations are computed as weighted averages of the concatenated embeddings from the selected samples, where weights are determined by each sample’s embedding proximity to the corresponding prototype. We achieve this via an optimal transport based clustering algorithm [74] that can enforce unique assignment and equipartition constraints across prototypes. To further stabilize prototype estimation and incorporate historical information, we apply an exponential moving average (EMA) [75] update scheme.

These above steps are iteratively executed throughout the curated pretraining process, enabling the model to progressively identify and emphasize informative, diverse, and under-represented samples. The data-curated pretraining procedure is summarized in Extended Data Algorithm 1. After pretraining, the resulting model can be directly applied to zero-shot evaluation in a non-adapted scheme or further fine-tuned with task-specific heads or decoders for a wide range of downstream tasks including classification, segmentation, and textual report generation.

4.5 Implementation details

CheXefficient, CheXfull, and CheXrandom share the same model architecture, training configuration, and hardware setup, and all models are trained for a total of 20 epochs for a fair comparison. The architecture follows a specific instantiation of the CLIP framework, consisting of an image encoder and a text encoder. We adopt DINOv2 [41] as the image encoder, using the [CLS] token representation, and BioClinicalBERT [42] as the text encoder. Both encoders are followed by a linear projection layer that maps image and text features into a shared embedding space of 512 dimensions. DINOv2 is implemented as a ViT-Base [76] model with 12 transformer blocks (approximately 86 million parameters), while BioClinicalBERT consists of 12 transformer layers with about 110 million parameters.

During pretraining, CXR images are resized to 378×378 before being fed into the image encoder. No data augmentation is applied to either image or text inputs. For the textual modality, the *Findings* and *Impression* sections of each radiology report are combined (when both are available), and used as input to the text encoder, with a maximum context length of 256 tokens. Model training is driven by an InfoNCE contrastive loss with a learnable temperature parameter, which is initialized to 0.01. The InfoNCE loss encourages alignment between paired CXR images and reports while

separating mismatched pairs. The number of prototypes $K = 6$, with a sensitivity analysis provided in Appendix B.2. Before starting the curation process, we warm up the prototypes by initializing them using k-means centroids [77] computed from 6,400 training samples. In the EMA update of prototypes, a smoothing factor of 0.1 is applied. In experiments, we observe that a single training epoch suffices to identify and curate representative samples from the full pretraining corpus, after which the curated subset is reused for the remaining epochs for improving efficiency. Optimization is conducted using the AdamW [78] optimizer with an initial learning rate of 5×10^{-5} , a weight decay of 1×10^{-4} , and a cosine annealing learning rate schedule. Since the most distant samples from each prototype may contain noise or outliers, e.g., corrupted images, severe artifacts, report translation errors, image-report mismatches, or template-generated reports with weak visual grounding, we first remove these extreme outliers (i.e., 5%) within each super-batch before performing the main curation step. Each super-batch contains 640 paired samples (8 GPUs \times 80 pairs per GPU). Notably, we find that CheXficient can also be trained on a single GPU by leveraging an embedding accumulation strategy, in which samples are repeatedly drawn from the pretraining set, their feature embeddings are extracted sequentially, and then accumulated to construct a large super-batch. This strategy can effectively enlarge the super-batch size without increasing the GPU count, enabling memory-efficient training while preserving the benefits of large-batch curation.

In fact, CheXficient introduces negligible additional pretraining overhead in comparison to each base model. The potentially increased overhead involves two major steps: 1) sample-prototype distance calculation: candidate training samples are drawn from in-batch data, which typically consists of only a few hundred samples, enabling efficient distance calculations to prototypes in the embedding space; 2) prototype update: new prototypes are obtained as weighted averages of embeddings from the selected samples and updated using an EMA scheme. This operation incurs minimal computational cost, as confirmed by our empirical observations.

4.6 Evaluation metrics

Classification performance is evaluated using well-established metrics widely adopted in prior studies [8, 52, 62], including the area under the receiver operating characteristic curve (AUROC) and the area under the precision-recall curve (AUPRC). AUROC characterizes the trade-off between the true positive rate (recall) and the false positive rate across varying decision thresholds, while AUPRC captures the trade-off between precision and recall. For multi-label classification, AUROC and AUPRC are computed independently for each disease category and then averaged to obtain the macro AUROC and macro AUPRC. Evaluation of retrieval tasks leverages the metric of Recall@1, which measures whether the exact paired radiology report is retrieved within the top-1 result for a given CXR image, and vice versa. Segmentation performance is evaluated using the Dice score, which quantifies pixel-wise overlap between the predicted segmentation maps and the corresponding ground-truth annotations. Performance of radiology report generation is evaluated using standard lexical metrics (BLEU-2, BLEU-4, and Rouge-L) which measure word-level overlap between the generated and reference reports, general semantic similarity metrics (BERTScore) that

measure contextual embedding-level semantic similarity between generated and reference reports, and radiology-specific metrics (RadGraph, Macro-F1-14, RaTEScore, and RadCliQ) which assess the clinical correctness and factual consistency of the generated reports.

4.7 Statistical analysis

To guarantee reliability and robustness of this study, we trained the model with five different random seeds and calculated the mean and standard deviation of the performance metrics, from which the standard error is computed as the standard deviation divided by $\sqrt{5}$. The corresponding 95% confidence interval (CI) is estimated as $1.96 \times$ the standard error. We perform two-sided paired t -tests to evaluate the statistical significance of performance differences between CheXficient and CheXfull, where metrics were computed across repeated experiments. A p -value less than 0.05 indicates a statistically significant difference, whereas a p -value greater than or equal to 0.05 suggests comparable performance between them. For feature-level kNN distance statistics, we use two-sided Welch’s t -test, as the distance distributions involve unequal sample sizes for the subset and full set.

4.8 Computation resources

All experiments were conducted on NVIDIA H100 GPUs with 80 GB memory. CheXficient required approximately 60 H100 GPU-hours for curation and pretraining on 280K paired CXR data, whereas CheXfull required about 220 H100 GPU-hours to train on 1,235K paired CXR data. For downstream fine-tuning, CheXficient used one H100 GPU for classification and segmentation tasks, and four H100 GPUs for radiology report generation. All pretraining and fine-tuning procedures were carefully monitored to ensure adequate convergence.

5 Data availability

All data used in this study are publicly available: MIMIC-CXR (<https://physionet.org/content/mimic-cxr-jpg/2.0.0/>); CheXpert (<https://stanfordmlgroup.github.io/competitions/chexpert/>); CheXpert-Plus (<https://aimi.stanford.edu/datasets/chexpert-plus>); ReXGradient-160K (<https://huggingface.co/datasets/rajpurkarlab/ReXGradient-160K>); PadChest (<https://bimcv.cipf.es/bimcv-projects/padchest/>); BIMCV-COVID19 (<https://bimcv.cipf.es/bimcv-projects/bimcv-covid19/>); CANDID-PTX (<https://figshare.com/articles/dataset/CANDID-PTX/14173982>); CASIA-CXR (<https://www.casia-cxr.net/>); Open-I (<https://openi.nlm.nih.gov/faq>); NIH ChestX-ray14 (<https://nihcc.app.box.com/v/ChestXray-NIHCC/folder/36938765345>); BRAX (<https://physionet.org/content/brax/1.1.0/>); VinDr-CXR (<https://vindr.ai/cxr>); VinDr-PCXR (<https://vindr.ai/datasets/pediatric-chest-x-ray>); ChestDR (https://springernature.figshare.com/articles/dataset/ChestDR_Thoracic_Diseases_Screening_in_Chest_Radiography/22302775); SIIM-PTX (www.kaggle.com/c/siim-acr-pneumothorax-segmentation); Pneumonia2017 (<https://data.mendeley.com/datasets/rscbjbr9sj/2>); TBX11K (<https://data.mendeley.com/datasets/tbx11k/1>).

[//datasetninja.com/tbx-11k](https://datasetninja.com/tbx-11k)); JSRT (<http://db.jsrt.or.jp/eng.php>); VinDr-RibCXR (<https://vindr.ai/ribcxr>).

6 Code availability

We have publicly released the data curation, pretraining, and evaluation code, along with the pretrained model weights, on GitHub at <https://github.com/cwangrun/CheXficient>. All experimental procedures are described in detail in the Methods section to support independent replication. To facilitate broader adoption, we also provide standardized downstream modeling tasks that are accessible to a wide scientific audience. Together, these resources are made available to ensure transparency and to promote further research in this area.

Acknowledgements

A.S.C. receives research support from the National Institutes of Health (grants - R01 HL167974, R01 AR077604, R01 EB002524, R01 AR079431, P41 EB027060, and contracts 75N92020C00008, 75N92020C00021); and from GE Healthcare, Philips, Amazon, Microsoft/OpenAI, and Stability.ai.

Author contributions

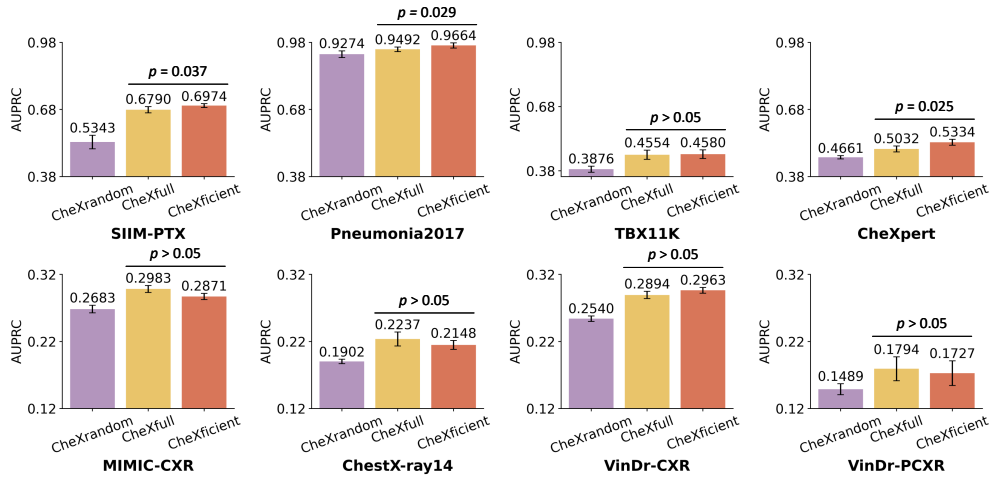
Conceptualization: C.W., Y.Z., A.S.C., C.P.L.; Methodology: C.W., Y.Z., Y.G., M.V., J.Liu, A.S.C., C.P.L.; AI model and code development: C.W., Y.Z.; Dataset development: C.W., Y.Z., Y.G.; Data analysis: C.W., Y.Z., Y.G., C.M., J.Long.; Writing - original draft, review, and editing: C.W., Y.Z., Y.G., M.V., C.M., J.Liu., F.P, J.Long., J.B.D, S.G., A.S.C., C.P.L.; Supervision: S.G., A.S.C., C.P.L.; Project administration: C.W., Y.Z., A.S.C., C.P.L.; Funding acquisition: A.S.C., C.P.L.

Declaration of interests

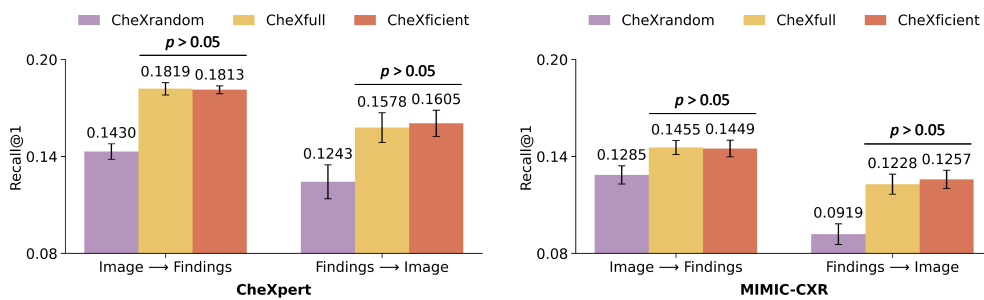
Jean-Benoit Delbrouck is an employee of hoppr.ai.

Extended Data Table 1 Comparative overview of CheXficient with other large-scale pretrained medical foundation models.

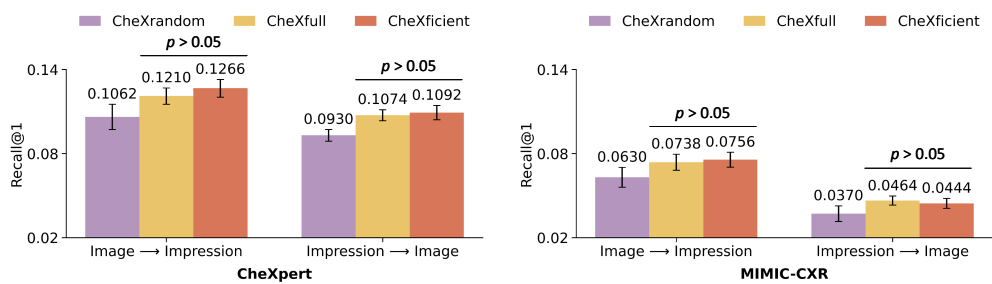
Model	Image encoder	Parameter size	Image resolution	Pretraining data size	Pretraining type	Data accessibility
CheXficient	ViT-Base	86 M	378×378	280 K	image-text	public
CheXZero [8]	ViT-Base	86 M	224×224	377 K	image-text	public
BioViL-T [79]	ResNet-50	25.6 M	512×512	377 K	image-text	public
LLaVA-Rad [54]	ViT-Base	86 M	518×518	697 K	image-text	public
RAD-DINO [62]	ViT-Base	86 M	518×518	883 K	self-supervised	public + private
CheXagent [52]	ViT-Large	307 M	512×512	1,077 K	image-text	public
Libra [63]	ViT-Base	86 M	518×518	1,213 K	self-supervised	public
MAIRA-2 [64]	ViT-Base	86 M	518×518	1,404 K	self-supervised	public + private
BiomedCLIP [9]	ViT-Base	86 M	224×224	15 M	image-text	private
RadFM [15]	12-layer 3D ViT	90 M	512×512	16 M	image-text	public + private
MedVersa [65]	Swin Transformer	88 M	224×224	29 M	image-text	public
MedGemma [16]	SoViT-400m	400 M	448×448	33 M	image-text	public + private



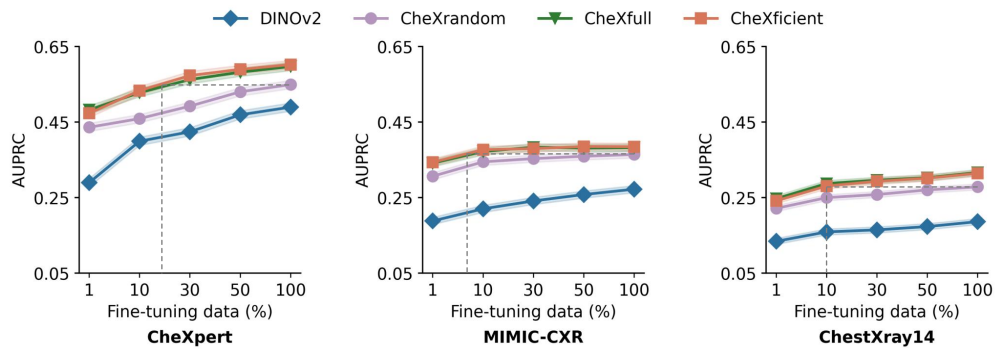
Extended Data Fig. 1 Performance (AUPRC) on zero-shot findings classification. We evaluate the pretrained models on 8 public datasets. Among them, SIIM-PTX, Pneumonia2017, and TBX11K are from external domains unseen in pretraining, while the remaining 5 datasets are used for internal evaluation. Compared to CheXfull, CheXficient achieves higher AUROC on 3 datasets ($p < 0.05$), and comparable performance on 5 datasets ($p > 0.05$). For each dataset, CheXficient outperforms CheXrandom by large margins. We present the mean \pm 95% confidence interval (CI) of AUPRC for each model. The listed p -values are calculated using two-sided t -tests.



Extended Data Fig. 2 Performance on zero-shot cross-modal retrieval (Image → Findings and Findings → Image). We evaluate the pretrained models on the public CheXpert and MIMIC-CXR benchmarks. CheXficient achieves performance comparable to CheXfull on both datasets ($p > 0.05$), while outperforming CheXrandom. We report the mean \pm 95% CI of Recall@1 (The recall of retrieving the exact paired CXR Findings section (or image) within the top-1 result for a given CXR image (or Findings section)).



Extended Data Fig. 3 Performance on zero-shot cross-modal retrieval (Image → Impression and Impression → Image). We evaluate the pretrained models on the public CheXpert and MIMIC-CXR benchmarks. CheXficient achieves performance comparable to CheXfull on both datasets ($p > 0.05$), while outperforming CheXrandom. We report the mean \pm 95% CI of Recall@1 (The recall of retrieving the exact paired CXR Impression section (or image) within the top-1 result for a given CXR image (or Impression section)).



Extended Data Fig. 4 Performance (AUPRC) comparison of CheXficient with other pretrained models in label-efficient disease prediction across three representative datasets: CheXpert ($n = 500$, 14 categories), MIMIC-CXR ($n = 3,082$, 14 categories), and ChestXray14 ($n = 25,596$, 15 categories). Performance is reported at varying proportions of labeled training data. Vertical dashed lines indicate the amount of labeled data required for CheXficient to match the performance of its counterpart CheXrandom.

Algorithm 1: Data-curated Pretraining Procedure of CheXficient

Data: Pretraining set $\mathcal{D} = \{(x_i^{\text{img}}, x_i^{\text{txt}})\}_{i=1}^{|\mathcal{D}|}$, number of training iterations T for curation, super-batch size $|\mathcal{S}|$, mini-batch size $|\mathcal{M}|$.

Result: Image encoder θ_{img} , text encoder θ_{txt} , curation set \mathcal{D}_c .

- 1 Initialize $\mathcal{D}_c = \emptyset$, initialize prototypes $\{\mathbf{p}_k\}_{k=1}^K$ by k-means;
 - 2 **for** *iteration* $t = 1$ **to** T **do**
 - 3 Given a large super-batch \mathcal{S} sampled from \mathcal{D} ;
 - 4 Extract unified embeddings $\mathbf{z}_i = \text{concat}(\mathbf{z}_i^{\text{img}}, \mathbf{z}_i^{\text{txt}})$ for each sample in \mathcal{S} ;
 - 5 Compute the distance of each \mathbf{z}_i to its nearest prototype: $\min_k \text{dist}(\mathbf{z}_i, \mathbf{p}_k)$;
 - 6 Select data based on sorted distances and form the mini-batch \mathcal{M} ;
 - 7 Contrastive pretraining on \mathcal{M} with InfoNCE loss;
 - 8 Calculate prototypes based on embeddings of the selected samples in \mathcal{M} ;
 - 9 Update prototypes $\{\mathbf{p}_k\}_{k=1}^K$ via exponential moving average;
 - 10 Add selected samples into the curation set: $\mathcal{D}_c = \mathcal{D}_c \cup \mathcal{M}$.
-

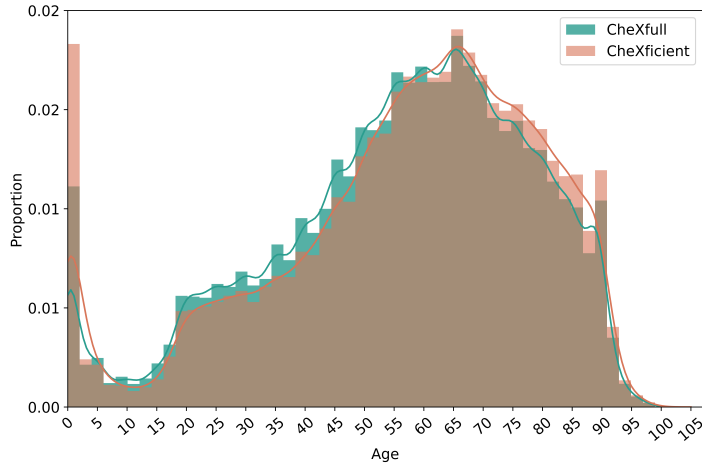


Figure A1 Distribution of patient age in the full training set (CheXfull) and the curated subset (CheXficient). The curated subset includes relatively more samples from two age groups: pediatric patients (0–5 years old) and older adults (over 65 years old).

Appendix A Additional analysis

To further investigate the effects of data curation in pretraining, we additionally analyze patient demographic information (e.g., age and race), distribution of frontal and lateral CXR scans, and distribution of token length of CXR reports.

A.1 Patient age

Patient demographic information is an important factor to consider when developing medical AI models. We examine how data curation during pretraining affects the distribution of patient age by comparing the full training set and the curated subset. Figure A1 shows that the curated subset tends to include relatively more samples from two age groups: pediatric patients (0–5 years old) and older adults (over 65 years old). This observation may be relevant because pediatric CXRs exhibit greater anatomical variability, and CXRs of older adults often show a wider range of age-related pathologies due to their higher prevalence in this population. Hence, the curated pretraining data emphasizes samples from these two age groups.

A.2 Patient race

Understanding the distribution of patient race in the training data helps assess whether curated pretraining could introduce unintended biases. We examine the distribution of patient race in the CheXpert dataset, which includes ‘White’, ‘Asian’, ‘Black’, ‘Pacific Islander’, ‘Native American’, and ‘Other’. Figure A2 shows that the distribution of races is similar between the full training set and the curated subset. This observation indicates that the curation process does not appear to be associated with patient race. This is consistent with prior work [62, 80], which points out that there is little detectable information about race and ethnicity in chest X-ray features.

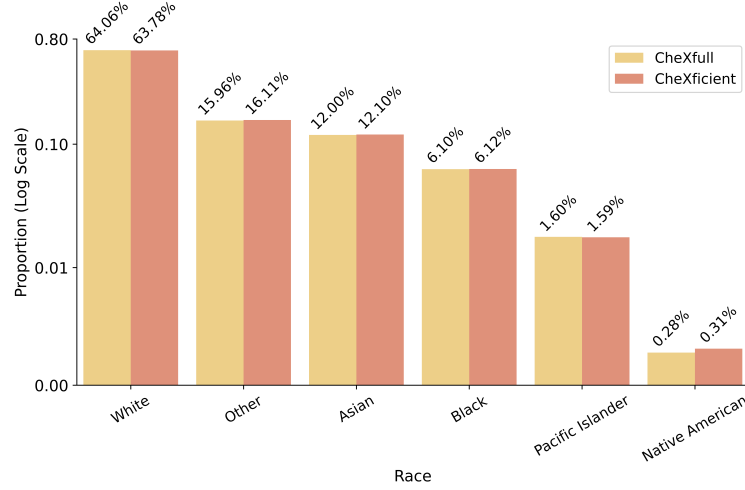


Figure A2 Distribution of patient race in the full training set (CheXfull) and the curated subset (CheXficient). The two sets show similar race distributions.

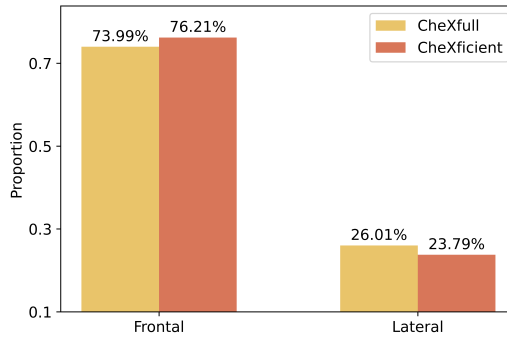


Figure A3 Distribution of frontal and lateral scans in the full training set (CheXfull) and the curated subset (CheXficient). The curated subset contains a higher proportion of frontal scans in comparison with the full training set.

A.3 Frontal and lateral CXR scans

Frontal and lateral chest X-rays (CXRs) are routinely acquired in clinical practice and are often jointly used to disambiguate radiological findings. We examine whether CheXficient exhibits a preference for either view during data curation. As shown in Figure A3, the curated subset contains a slightly higher proportion of frontal scans than the original dataset. One possible explanation is that frontal CXRs may provide more informative visual cues for many radiological findings, whereas certain findings are less clearly visible on lateral scans [81]. This observation suggests that the curation process tends to prioritize the informative frontal scans during pretraining.

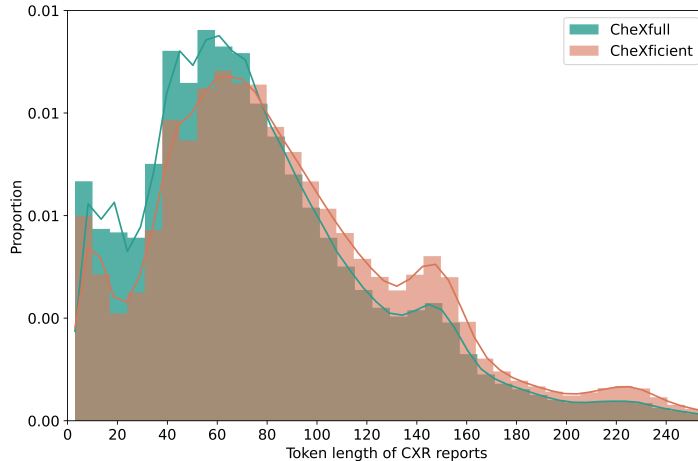


Figure A4 Distribution of CXR report token lengths in the full training set (CheXfull) and the curated subset (CheXficient). The curated subset demonstrates a higher proportion of longer CXR reports with high informativeness.

A.4 Token length of CXR reports

We further analyze the token length of CXR reports as a proxy for the informativeness of training samples. In general, CXR reports describing normal findings tend to be shorter, whereas those containing rich pathological findings require more detailed descriptions. As shown in Figure A4, the curated subset exhibits a relatively higher proportion of longer CXR reports, suggesting that the data curation process systematically favors samples with more informative clinical descriptions.

Appendix B Ablation study

To showcase the advantages of the CheXficient framework, we conduct ablation studies to highlight its multimodal embedding design (Section B.1). We further evaluate its robustness through a sensitivity analysis with respect to the number of prototypes (Section B.2).

B.1 Multimodal embedding vs. unimodal embedding

In CheXficient, data curation can be performed using either unified multimodal embeddings obtained by concatenating image and text features, i.e., $\text{concat}(\mathbf{z}_i^{\text{img}}, \mathbf{z}_i^{\text{txt}})$, or unimodal embeddings derived from images ($\mathbf{z}_i^{\text{img}}$) or reports ($\mathbf{z}_i^{\text{txt}}$) alone. Table B1 presents an ablation study comparing these choices. While no consistent trend is observed indicating the superiority of a single modality, combining image and text embeddings generally yields better performance than using either modality alone. This suggests that paired image-report data provide richer, complementary semantic cues that more accurately reflect data importance for effective data selection, ultimately contributing to improved representation learning.

Table B1 Effect of different feature embeddings used in CheXficient pretraining, e.g., image-only $\mathbf{z}_i^{\text{img}}$, text-only $\mathbf{z}_i^{\text{txt}}$, and image-text concatenation $\text{concat}(\mathbf{z}_i^{\text{img}}, \mathbf{z}_i^{\text{txt}})$, on 280K curated CXR data pairs. Zero-shot findings classification performance (AUROC) is reported across eight datasets.

Dataset	$\mathbf{z}_i^{\text{img}}$	$\mathbf{z}_i^{\text{txt}}$	$\text{concat}(\mathbf{z}_i^{\text{img}}, \mathbf{z}_i^{\text{txt}})$
SIIM-PTX	0.8920 [0.8858, 0.8981]	0.8937 [0.8900, 0.8975]	0.9074 [0.9001, 0.9148]
Pneumonia2017	0.9481 [0.9416, 0.9546]	0.9490 [0.9447, 0.9532]	0.9659 [0.9597, 0.9722]
TBX11K	0.8209 [0.8145, 0.8274]	0.8174 [0.8110, 0.8238]	0.8248 [0.8183, 0.8313]
CheXpert	0.8407 [0.8361, 0.8453]	0.8335 [0.8290, 0.8380]	0.8535 [0.8501, 0.8569]
MIMIC-CXR	0.6613 [0.6558, 0.6669]	0.6758 [0.6708, 0.6807]	0.6866 [0.6824, 0.6908]
ChestX-ray14	0.7191 [0.7166, 0.7216]	0.7312 [0.7255, 0.7369]	0.7308 [0.7281, 0.7336]
VinDr-CXR	0.8966 [0.8929, 0.9003]	0.8927 [0.8866, 0.8989]	0.9005 [0.8929, 0.9081]
VinDr-PCXR	0.6992 [0.6915, 0.7070]	0.6956 [0.6882, 0.7031]	0.7019 [0.6951, 0.7087]

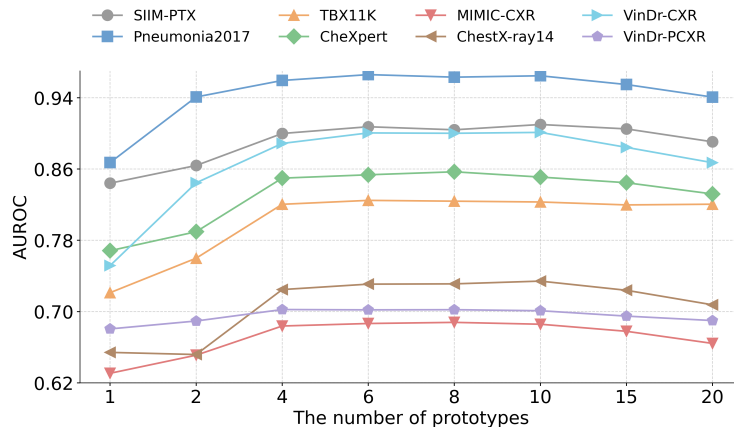


Figure B5 Effect of the number of prototypes used in CheXficient pretraining on zero-shot findings classification performance across eight datasets.

B.2 Effect of the number of prototypes

We further analyze the sensitivity of CheXficient to the number of prototypes K , as shown in Figure B5, by varying K under the same pretraining data budget (i.e., 280K data pairs). Overall, the zero-shot findings classification performance is relatively robust when K ranges from 4 to 10. Using too few prototypes fails to adequately capture the complexity and diversity of the training data, leading to sub-optimal performance. In contrast, employing an excessive number of prototypes introduces surplus or even harmful information, resulting in performance degradation and increased model complexity. Based on these observations, we set the number of prototypes to $K = 6$ for all remaining experiments.

Appendix C Downstream implementation details

The implementation details for training and evaluating each downstream model are described below.

C.1 Image classification

All downstream image classification experiments are conducted on a single NVIDIA H100 GPU. We use a batch size of 512 and optimize the models with AdamW, using a base learning rate of 3×10^{-2} , a weight decay of 1×10^{-4} , and a step-based learning rate decay scheduler. For image pre-processing, we apply center cropping and no additional image augmentation is applied during downstream training. CXR image intensities are normalized using a mean of [0.4814, 0.4578, 0.4082] and a standard deviation of [0.2686, 0.2613, 0.2757]. All classification models are trained for 15 epochs. The final checkpoint is used for inference on the test set, as no overfitting is observed based on the validation loss. We conduct experiments over five runs with different random seeds. Under this GPU setup, fine-tuning a linear classification head on top of the visual encoder takes approximately 0.41 seconds per iteration.

C.2 Semantic segmentation

We evaluate the segmentation tasks on 1 NVIDIA H100 GPU. We use a training batch size of 256, AdamW optimizer, a base learning rate of 3×10^{-4} , a weight decay of 1×10^{-4} , and a step-based learning rate decay scheduler. For image pre-processing, we apply center cropping and no additional image augmentation is applied during downstream training. CXR image intensities are normalized using a mean of [0.4814, 0.4578, 0.4082] and a standard deviation of [0.2686, 0.2613, 0.2757]. The segmentation models are trained for a total of 120 epochs, using a combined Dice loss and cross-entropy loss as the training objective. For lung segmentation on the JSRT dataset, we use a data split of 172/25/50 for the training, validation, and test sets, respectively, and report Dice scores on the test set. For pneumothorax segmentation on SIIM-PTX and rib segmentation on VinDr-RibCXR, we follow the official data splits provided by the datasets. The model with the lowest validation loss is selected for evaluation on the test set. Under the given GPU setup, training a U-Net decoder as the segmentation head on top of the visual encoder takes approximately 0.45 seconds per iteration.

C.3 Radiology report generation

All radiology report generation experiments are conducted on 1 compute node equipped with 4 NVIDIA H100 GPUs (80GB each). We follow the same training hyper-parameters as LLaVA-Rad [54]. Specifically, we use a total batch size of 128 (32 per GPU), a cosine learning rate scheduler with a warmup phase over 3% of the training steps, and a base learning rate of 3×10^{-5} . We adopt a two-stage fine-tuning strategy over three epochs, where the image encoder is kept frozen throughout both stages. In the first stage (feature alignment), both the image encoder and the large language model (LLM) are frozen, and only the MLP projection layer is trained. In the second stage (end-to-end fine-tuning), the MLP projection layer and the LLM are

jointly updated, while the image encoder remains frozen. Training on MIMIC-CXR and ReXGradient-160K requires approximately 0.5 and 0.2 days, respectively.

References

- [1] Bommasani, R.: On the opportunities and risks of foundation models. arXiv preprint arXiv:2108.07258 (2021)
- [2] Moor, M., Banerjee, O., Abad, Z.S.H., Krumholz, H.M., Leskovec, J., Topol, E.J., Rajpurkar, P.: Foundation models for generalist medical artificial intelligence. *Nature* **616**(7956), 259–265 (2023)
- [3] Khan, W., Leem, S., See, K.B., Wong, J.K., Zhang, S., Fang, R.: A comprehensive survey of foundation models in medicine. *IEEE Reviews in Biomedical Engineering* (2025)
- [4] Wiggins, W.F., Tejani, A.S.: On the opportunities and risks of foundation models for natural language processing in radiology. *Radiology: Artificial Intelligence* **4**(4), 220119 (2022)
- [5] Lu, M.Y., Chen, B., Williamson, D.F., Chen, R.J., Liang, I., Ding, T., Jaume, G., Odintsov, I., Le, L.P., Gerber, G., *et al.*: A visual-language foundation model for computational pathology. *Nature medicine* **30**(3), 863–874 (2024)
- [6] Yan, S., Yu, Z., Primiero, C., Vico-Alonso, C., Wang, Z., Yang, L., Tschandl, P., Hu, M., Ju, L., Tan, G., *et al.*: A multimodal vision foundation model for clinical dermatology. *Nature Medicine*, 1–12 (2025)
- [7] Zhou, Y., Chia, M.A., Wagner, S.K., Ayhan, M.S., Williamson, D.J., Struyven, R.R., Liu, T., Xu, M., Lozano, M.G., Woodward-Court, P., *et al.*: A foundation model for generalizable disease detection from retinal images. *Nature* **622**(7981), 156–163 (2023)
- [8] Tiu, E., Talius, E., Patel, P., Langlotz, C.P., Ng, A.Y., Rajpurkar, P.: Expert-level detection of pathologies from unannotated chest x-ray images via self-supervised learning. *Nature biomedical engineering* **6**(12), 1399–1406 (2022)
- [9] Zhang, S., Xu, Y., Usuyama, N., Xu, H., Bagga, J., Tinn, R., Preston, S., Rao, R., Wei, M., Valluri, N., *et al.*: Biomedclip: a multimodal biomedical foundation model pretrained from fifteen million scientific image-text pairs. arXiv preprint arXiv:2303.00915 (2023)
- [10] Lozano, A., Sun, M.W., Burgess, J., Chen, L., Nirschl, J.J., Gu, J., Lopez, I., Aklilu, J., Rau, A., Katzer, A.W., *et al.*: Biomedica: An open biomedical image-caption archive, dataset, and vision-language models derived from scientific literature. In: *Proceedings of the Computer Vision and Pattern Recognition Conference*, pp. 19724–19735 (2025)
- [11] Huang, Z., Bianchi, F., Yuksekgonul, M., Montine, T.J., Zou, J.: A visual-language foundation model for pathology image analysis using medical twitter.

Nature medicine **29**(9), 2307–2316 (2023)

- [12] He, Y., Huang, F., Jiang, X., Nie, Y., Wang, M., Wang, J., Chen, H.: Foundation model for advancing healthcare: Challenges, opportunities and future directions. *IEEE Reviews in Biomedical Engineering* (2024)
- [13] Acosta, J.N., Falcone, G.J., Rajpurkar, P., Topol, E.J.: Multimodal biomedical ai. *Nature medicine* **28**(9), 1773–1784 (2022)
- [14] Zhou, S.K., Greenspan, H., Davatzikos, C., Duncan, J.S., Van Ginneken, B., Madabhushi, A., Prince, J.L., Rueckert, D., Summers, R.M.: A review of deep learning in medical imaging: Imaging traits, technology trends, case studies with progress highlights, and future promises. *Proceedings of the IEEE* **109**(5), 820–838 (2021)
- [15] Wu, C., Zhang, X., Zhang, Y., Hui, H., Wang, Y., Xie, W.: Towards generalist foundation model for radiology by leveraging web-scale 2d&3d medical data. *Nature Communications* **16**(1), 7866 (2025)
- [16] Sellergren, A., Kazemzadeh, S., Jaroensri, T., Kiraly, A., Traverse, M., Kohlberger, T., Xu, S., Jamil, F., Hughes, C., Lau, C., et al.: Medgemma technical report. *arXiv preprint arXiv:2507.05201* (2025)
- [17] Joshi, S., Jain, A., Payani, A., Mirzasoleiman, B.: Data-efficient contrastive language-image pretraining: Prioritizing data quality over quantity. In: *International Conference on Artificial Intelligence and Statistics*, pp. 1000–1008 (2024). PMLR
- [18] Gadre, S.Y., Ilharco, G., Fang, A., Hayase, J., Smyrnis, G., Nguyen, T., Marten, R., Wortsman, M., Ghosh, D., Zhang, J., et al.: Datacomp: In search of the next generation of multimodal datasets. *Advances in Neural Information Processing Systems* **36**, 27092–27112 (2023)
- [19] Cherti, M., Beaumont, R., Wightman, R., Wortsman, M., Ilharco, G., Gordon, C., Schuhmann, C., Schmidt, L., Jitsev, J.: Reproducible scaling laws for contrastive language-image learning. In: *Proceedings of the IEEE/CVF Conference on Computer Vision and Pattern Recognition*, pp. 2818–2829 (2023)
- [20] Mindermann, S., Brauner, J.M., Razzak, M.T., Sharma, M., Kirsch, A., Xu, W., Höltgen, B., Gomez, A.N., Morisot, A., Farquhar, S., et al.: Prioritized training on points that are learnable, worth learning, and not yet learnt. In: *International Conference on Machine Learning*, pp. 15630–15649 (2022). PMLR
- [21] Sorscher, B., Geirhos, R., Shekhar, S., Ganguli, S., Morcos, A.: Beyond neural scaling laws: beating power law scaling via data pruning. *Advances in Neural Information Processing Systems* **35**, 19523–19536 (2022)
- [22] Wang, A.J., Lin, K.Q., Zhang, D.J., Lei, S.W., Shou, M.Z.: Too large; data

- reduction for vision-language pre-training. In: Proceedings of the IEEE/CVF International Conference on Computer Vision, pp. 3147–3157 (2023)
- [23] Goyal, S., Maini, P., Lipton, Z.C., Raghunathan, A., Kolter, J.Z.: Scaling laws for data filtering—data curation cannot be compute agnostic. In: Proceedings of the IEEE/CVF Conference on Computer Vision and Pattern Recognition, pp. 22702–22711 (2024)
- [24] Oord, A.v.d., Li, Y., Vinyals, O.: Representation learning with contrastive predictive coding. arXiv preprint arXiv:1807.03748 (2018)
- [25] Radford, A., Kim, J.W., Hallacy, C., Ramesh, A., Goh, G., Agarwal, S., Sastry, G., Askell, A., Mishkin, P., Clark, J., *et al.*: Learning transferable visual models from natural language supervision. In: International Conference on Machine Learning, pp. 8748–8763 (2021). PmLR
- [26] Zhou, T., Wang, W., Konukoglu, E., Van Gool, L.: Rethinking semantic segmentation: A prototype view. In: Proceedings of the IEEE/CVF Conference on Computer Vision and Pattern Recognition, pp. 2582–2593 (2022)
- [27] Wang, C., Chen, Y., Liu, F., Liu, Y., McCarthy, D.J., Frazer, H., Carneiro, G.: Mixture of gaussian-distributed prototypes with generative modelling for interpretable and trustworthy image recognition. *IEEE Transactions on Pattern Analysis and Machine Intelligence* (2025)
- [28] Chambon, P., Delbrouck, J.-B., Sounack, T., Huang, S.-C., Chen, Z., Varma, M., Truong, S.Q., Chuong, C.T., Langlotz, C.P.: Chexpert plus: Augmenting a large chest x-ray dataset with text radiology reports, patient demographics and additional image formats. arXiv preprint arXiv:2405.19538 (2024)
- [29] Johnson, A.E., Pollard, T.J., Berkowitz, S.J., Greenbaum, N.R., Lungren, M.P., Deng, C.-y., Mark, R.G., Horng, S.: MIMIC-CXR, a de-identified publicly available database of chest radiographs with free-text reports. *Scientific data* **6**(1), 317 (2019)
- [30] Zhang, X., Acosta, J.N., Miller, J., Huang, O., Rajpurkar, P.: Rexgradient-160k: A large-scale publicly available dataset of chest radiographs with free-text reports. arXiv preprint arXiv:2505.00228 (2025)
- [31] Bustos, A., Pertusa, A., Salinas, J.-M., De La Iglesia-Vaya, M.: Padchest: A large chest x-ray image dataset with multi-label annotated reports. *Medical image analysis* **66**, 101797 (2020)
- [32] Vayá, M.D.L.I., Saborit, J.M., Montell, J.A., Pertusa, A., Bustos, A., Cazorla, M., Galant, J., Barber, X., Orozco-Beltrán, D., García-García, F., *et al.*: Bimcv covid-19+: A large annotated dataset of rx and ct images from covid-19 patients. arXiv preprint arXiv:2006.01174 (2020)

- [33] Feng, S., Azzollini, D., Kim, J.S., Jin, C.-K., Gordon, S.P., Yeoh, J., Kim, E., Han, M., Lee, A., Patel, A., *et al.*: Curation of the candid-ptx dataset with free-text reports. *Radiology: Artificial Intelligence* **3**(6), 210136 (2021)
- [34] Metmer, H., Yang, X.: An open chest x-ray dataset with benchmarks for automatic radiology report generation in french. *Neurocomputing* **609**, 128478 (2024)
- [35] Demner-Fushman, D., Kohli, M.D., Rosenman, M.B., Shooshan, S.E., Rodriguez, L., Antani, S., Thoma, G.R., McDonald, C.J.: Preparing a collection of radiology examinations for distribution and retrieval. *Journal of the American Medical Informatics Association* **23**(2), 304–310 (2015)
- [36] Wang, X., Peng, Y., Lu, L., Lu, Z., Bagheri, M., Summers, R.M.: Chestx-ray8: Hospital-scale chest x-ray database and benchmarks on weakly-supervised classification and localization of common thorax diseases. In: *Proceedings of the IEEE Conference on Computer Vision and Pattern Recognition*, pp. 2097–2106 (2017)
- [37] Reis, E.P., De Paiva, J.P., Da Silva, M.C., Ribeiro, G.A., Paiva, V.F., Bulgarelli, L., Lee, H.M., Santos, P.V., Brito, V.M., Amaral, L.T., *et al.*: Brax, brazilian labeled chest x-ray dataset. *Scientific Data* **9**(1), 487 (2022)
- [38] Nguyen, H.Q., Lam, K., Le, L.T., Pham, H.H., Tran, D.Q., Nguyen, D.B., Le, D.D., Pham, C.M., Tong, H.T., Dinh, D.H., *et al.*: Vindr-cxr: An open dataset of chest x-rays with radiologist’s annotations. *Scientific Data* **9**(1), 429 (2022)
- [39] Pham, H.H., Nguyen, N.H., Tran, T.T., Nguyen, T.N., Nguyen, H.Q.: Pedicxr: an open, large-scale chest radiograph dataset for interpretation of common thoracic diseases in children. *Scientific Data* **10**(1), 240 (2023)
- [40] Wang, D., Wang, X., Wang, L., Li, M., Da, Q., Liu, X., Gao, X., Shen, J., He, J., Shen, T., *et al.*: A real-world dataset and benchmark for foundation model adaptation in medical image classification. *Scientific Data* **10**(1), 574 (2023)
- [41] Oquab, M., Darcet, T., Moutakanni, T., Vo, H., Szafraniec, M., Khalidov, V., Fernandez, P., Haziza, D., Massa, F., El-Nouby, A., *et al.*: Dinov2: Learning robust visual features without supervision. *arXiv preprint arXiv:2304.07193* (2023)
- [42] Alsentzer, E., Murphy, J.R., Boag, W., Weng, W.-H., Jin, D., Naumann, T., McDermott, M.: Publicly available clinical bert embeddings. *arXiv preprint arXiv:1904.03323* (2019)
- [43] Abdi, H., Williams, L.J.: Principal component analysis. *Wiley interdisciplinary reviews: computational statistics* **2**(4), 433–459 (2010)
- [44] Zawacki, A., Wu, C., Shih, G., Elliott, J., Fomitchev, M., Hussain, M., Lakhani, P., Culliton, P., Bao, S.: SIIM-ACR Pneumothorax Segmentation 2019. <https://www.siemens-healthineers.com/academic-scholarship>

[//www.kaggle.com/competitions/siim-acr-pneumothorax-segmentation/](https://www.kaggle.com/competitions/siim-acr-pneumothorax-segmentation/)

- [45] Kermany, D.: Labeled optical coherence tomography (oct) and chest x-ray images for classification. Mendeley data (2018)
- [46] Liu, Y., Wu, Y.-H., Ban, Y., Wang, H., Cheng, M.-M.: Rethinking computer-aided tuberculosis diagnosis. In: Proceedings of the IEEE/CVF Conference on Computer Vision and Pattern Recognition, pp. 2646–2655 (2020)
- [47] Ma, D., Pang, J., Gotway, M.B., Liang, J.: A fully open ai foundation model applied to chest radiography. *Nature*, 1–11 (2025)
- [48] Wang, C., Liu, F., Chen, Y., Frazer, H., Carneiro, G.: Cross-and intra-image prototypical learning for multi-label disease diagnosis and interpretation. *IEEE Transactions on Medical Imaging* (2025)
- [49] Shiraishi, J., Katsuragawa, S., Ikezoe, J., Matsumoto, T., Kobayashi, T., Komatsu, K.-i., Matsui, M., Fujita, H., Kodera, Y., Doi, K.: Development of a digital image database for chest radiographs with and without a lung nodule: receiver operating characteristic analysis of radiologists’ detection of pulmonary nodules. *American journal of roentgenology* **174**(1), 71–74 (2000)
- [50] Nguyen, H.C., Le, T.T., Pham, H.H., Nguyen, H.Q.: Vindr-ribcyr: A benchmark dataset for automatic segmentation and labeling of individual ribs on chest x-rays. arXiv preprint arXiv:2107.01327 (2021)
- [51] Ronneberger, O., Fischer, P., Brox, T.: U-net: Convolutional networks for biomedical image segmentation. In: International Conference on Medical Image Computing and Computer-assisted Intervention, pp. 234–241 (2015). Springer
- [52] Chen, Z., Varma, M., Delbrouck, J.-B., Paschali, M., Blankemeier, L., Van Veen, D., Valanarasu, J.M.J., Youssef, A., Cohen, J.P., Reis, E.P., et al.: Chexagent: Towards a foundation model for chest x-ray interpretation. arXiv preprint arXiv:2401.12208 (2024)
- [53] Liu, H., Li, C., Wu, Q., Lee, Y.J.: Visual instruction tuning. *Advances in neural information processing systems* **36**, 34892–34916 (2023)
- [54] Zambrano Chaves, J.M., Huang, S.-C., Xu, Y., Xu, H., Usuyama, N., Zhang, S., Wang, F., Xie, Y., Khademi, M., Yang, Z., et al.: A clinically accessible small multimodal radiology model and evaluation metric for chest x-ray findings. *Nature Communications* **16**(1), 3108 (2025)
- [55] Chiang, W.-L., Li, Z., Lin, Z., Sheng, Y., Wu, Z., Zhang, H., Zheng, L., Zhuang, S., Zhuang, Y., Gonzalez, J.E., et al.: Vicuna: An open-source chatbot impressing gpt-4 with 90%* chatgpt quality. See <https://vicuna.lmsys.org> (accessed 14 April 2023) **2**(3), 6 (2023)

- [56] Papineni, K., Roukos, S., Ward, T., Zhu, W.-J.: Bleu: a method for automatic evaluation of machine translation. In: Proceedings of the 40th Annual Meeting of the Association for Computational Linguistics, pp. 311–318 (2002)
- [57] Lin, C.-Y.: Rouge: A package for automatic evaluation of summaries. In: Text Summarization Branches Out, pp. 74–81 (2004)
- [58] Delbrouck, J.-B., Chambon, P., Bluethgen, C., Tsai, E., Almusa, O., Langlotz, C.: Improving the factual correctness of radiology report generation with semantic rewards. In: Findings of the Association for Computational Linguistics: EMNLP 2022, pp. 4348–4360 (2022)
- [59] Yu, F., Endo, M., Krishnan, R., Pan, I., Tsai, A., Reis, E.P., Fonseca, E.K.U.N., Lee, H.M.H., Abad, Z.S.H., Ng, A.Y., et al.: Evaluating progress in automatic chest x-ray radiology report generation. *Patterns* **4**(9) (2023)
- [60] Zhao, W., Wu, C., Zhang, X., Zhang, Y., Wang, Y., Xie, W.: Ratescore: A metric for radiology report generation. arXiv preprint arXiv:2406.16845 (2024)
- [61] Zhang, T., Kishore, V., Wu, F., Weinberger, K.Q., Artzi, Y.: Bertscore: Evaluating text generation with bert. arXiv preprint arXiv:1904.09675 (2019)
- [62] Perez-Garcia, F., Sharma, H., Bond-Taylor, S., Bouzid, K., Salvatelli, V., Ilse, M., Bannur, S., Castro, D.C., Schwaighofer, A., Lungren, M.P., *et al.*: Exploring scalable medical image encoders beyond text supervision. *Nature Machine Intelligence* **7**(1), 119–130 (2025)
- [63] Zhang, X., Meng, Z., Lever, J., Ho, E.S.: Libra: Leveraging temporal images for biomedical radiology analysis. In: Findings of the Association for Computational Linguistics: ACL 2025, pp. 17275–17303 (2025)
- [64] Bannur, S., Bouzid, K., Castro, D.C., Schwaighofer, A., Thieme, A., Bond-Taylor, S., Ilse, M., Pérez-García, F., Salvatelli, V., Sharma, H., et al.: Maira-2: Grounded radiology report generation. arXiv preprint arXiv:2406.04449 (2024)
- [65] Zhou, H.-Y., Acosta, J.N., Adithan, S., Datta, S., Topol, E.J., Rajpurkar, P.: Medversa: A generalist foundation model for medical image interpretation. arXiv preprint arXiv:2405.07988 (2024)
- [66] Bluethgen, C., Chambon, P., Delbrouck, J.-B., Van Der Sluijs, R., Połacin, M., Zambrano Chaves, J.M., Abraham, T.M., Purohit, S., Langlotz, C.P., Chaudhari, A.S.: A vision–language foundation model for the generation of realistic chest x-ray images. *Nature Biomedical Engineering* **9**(4), 494–506 (2025)
- [67] Sun, Y., Tan, W., Gu, Z., He, R., Chen, S., Pang, M., Yan, B.: A data-efficient strategy for building high-performing medical foundation models. *Nature Biomedical Engineering*, 1–13 (2025)

- [68] Hu, X., Gu, L., Kobayashi, K., Liu, L., Zhang, M., Harada, T., Summers, R.M., Zhu, Y.: Interpretable medical image visual question answering via multi-modal relationship graph learning. *Medical Image Analysis* **97**, 103279 (2024)
- [69] Liu, B., Zou, K., Zhan, L.-M., Lu, Z., Dong, X., Chen, Y., Xie, C., Cao, J., Wu, X.-M., Fu, H.: Gemex: A large-scale, groundable, and explainable medical vqa benchmark for chest x-ray diagnosis. In: *Proceedings of the IEEE/CVF International Conference on Computer Vision*, pp. 21310–21320 (2025)
- [70] Huy, T.D., Huynh, D.A., Xie, Y., Qi, Y., Chen, Q., Le Nguyen, P., Tran, S.K., Phung, S.L., Hengel, A., Liao, Z., *et al.*: Seeing the trees for the forest: rethinking weakly-supervised medical visual grounding. In: *Proceedings of the IEEE/CVF International Conference on Computer Vision*, pp. 24445–24455 (2025)
- [71] Huang, S.-C., Shen, L., Lungren, M.P., Yeung, S.: Gloria: A multimodal global-local representation learning framework for label-efficient medical image recognition. In: *Proceedings of the IEEE/CVF International Conference on Computer Vision*, pp. 3942–3951 (2021)
- [72] You, K., Gu, J., Ham, J., Park, B., Kim, J., Hong, E.K., Baek, W., Roh, B.: Cxr-clip: Toward large scale chest x-ray language-image pre-training. In: *International Conference on Medical Image Computing and Computer-Assisted Intervention*, pp. 101–111 (2023). Springer
- [73] Eldar, Y., Lindenbaum, M., Porat, M., Zeevi, Y.Y.: The farthest point strategy for progressive image sampling. *IEEE transactions on image processing* **6**(9), 1305–1315 (1997)
- [74] Cuturi, M.: Sinkhorn distances: Lightspeed computation of optimal transport. *Advances in neural information processing systems* **26** (2013)
- [75] Hunter, J.S.: The exponentially weighted moving average. *Journal of Quality Technology* **18**(4), 203–210 (1986)
- [76] Dosovitskiy, A.: An image is worth 16x16 words: Transformers for image recognition at scale. *arXiv preprint arXiv:2010.11929* (2020)
- [77] Hartigan, J.A., Wong, M.A.: Algorithm as 136: A k-means clustering algorithm. *Journal of the royal statistical society. series c (applied statistics)* **28**(1), 100–108 (1979)
- [78] Loshchilov, I., Hutter, F., *et al.*: Fixing weight decay regularization in adam. *arXiv preprint arXiv:1711.05101* **5**(5), 5 (2017)
- [79] Bannur, S., Hyland, S., Liu, Q., Perez-Garcia, F., Ilse, M., Castro, D.C., Boecking, B., Sharma, H., Bouzid, K., Thieme, A., *et al.*: Learning to exploit temporal structure for biomedical vision-language processing. In: *Proceedings of the IEEE/CVF*

Conference on Computer Vision and Pattern Recognition, pp. 15016–15027 (2023)

- [80] Duffy, G., Clarke, S.L., Christensen, M., He, B., Yuan, N., Cheng, S., Ouyang, D.: Confounders mediate ai prediction of demographics in medical imaging. *NPJ digital medicine* **5**(1), 188 (2022)
- [81] Hashir, M., Bertrand, H., Cohen, J.P.: Quantifying the value of lateral views in deep learning for chest x-rays. In: *Medical Imaging with Deep Learning*, pp. 288–303 (2020). PMLR